Journal of Sound and Vibration 619 (2025) 119360

Contents lists available at ScienceDirect

Journal of Sound and Vibration

journal homepage: www.elsevier.com/locate/jsvi

Spatial-temporal evolution prediction of train-induced settlement in railway transition zone using a simplified iterative framework

Borong Peng [a], Karel N. Van Dalen [b], Zheng Li [a,*], Sakdirat Kaewunruen [c], Lei Xu [a], Jim Shiau [d], Tao Lu [e]

[a] School of Civil Engineering, Central South University, Changsha 410075, China
[b] Faculty of Civil Engineering and Geosciences, Delft University of Technology, Delft 2628CN; Netherlands;
[c] Department of Civil Engineering, School of Engineering, University of Birmingham, Birmingham, B152TT, United Kingdom
[d] School of Engineering, University of Southern Queensland, Toowoomba, 4350, QLD, Australia;
[e] SWJTU-Leeds Joint School, Southwest Jiaotong University, 611756 Chengdu, China.

ARTICLE INFO

Keywords:
Transition zone
Settlement prediction
Train-track-substructure interaction
Time-frequency analysis

ABSTRACT

Accurate prediction of train-induced settlement in railway transition zones is of paramount importance for ensuring the safety and serviceability of high-speed railway (HSR) infrastructure. The inherent complexity of mechanical properties and settlement distribution in these zones stems from the significant stiffness variation between different track structures. This study presents a novel iterative framework for long-term settlement prediction specifically tailored to ballastless track transition zones of HSR systems. The framework couples a dynamic Train-Track-Transition Zone (TTTZ) model with a plastic strain prediction model for soil, enhanced by a jump-step iterative algorithm that improves computational efficiency while maintaining accuracy. The model's validity has been verified through comprehensive comparisons with in-situ measurements and existing analytical solutions. Numerical results demonstrate that the iterative updating of track irregularities is crucial for accurate settlement prediction, as it accounts for the time-dependent dynamic characteristics of the TTTZ system. Furthermore, a wavelet transform-short energy method is developed to identify high-density vibration energy distributions in the spatial domain, establishing a robust correlation between dynamic responses and settlement evolution. This study underscores the importance of iterative modeling and advanced time-frequency analysis in settlement prediction and track quality assessment, offering valuable insights for the design, maintenance, and evaluation of HSR transition zones.

1. Introduction

Settlements of railway tracks during operation are usually related to the cumulative loading cycles imposed by passing trains [1–4]. Due to variations of structural stiffness, railway transition zones often experience more rapid track degradation than regular sections [4–7], primarily attributed to transition radiation which occurs in the vicinity of transition zones [8,9]. To assure the safety of vehicles and the comfort of passengers, railway tracks at transition zones need to be maintained up to 3 to 8 times more frequently than in normal subgrade zones when dealing with settlement issues. As reported in [4], settlement not only deteriorates track geometry but

* Corresponding author.
E-mail address: lizheng0924@csu.edu.cn (Z. Li).

https://doi.org/10.1016/j.jsv.2025.119360
Received 4 August 2024; Received in revised form 24 July 2025; Accepted 25 July 2025
Available online 27 July 2025

also intensifies train-track dynamic interaction. Therefore, the prediction of train-induced settlement in railway transition zones is essential for running safety and riding comfort. The settlement in transition zones develops over time due to repeated train loading, exhibiting pronounced long-term behavior that must be quantified and assessed during the life cycle. Furthermore, the behavior of the train-track interaction during the settlement evolution needs to be investigated for the demand of train running safety.

In recent years, considerable research has been devoted to preventive measures and condition monitoring for settlement in transition zones. For example, Chumyen et al. [10] proposed measures to improve transition zone performance through soil reinforcement and auxiliary rails, demonstrating that soil improvement yields more effective mitigation of dynamic responses. Jain et al. [11] evaluated the efficacy of the most commonly used mitigation method and proposed a novel Safe Hull-Inspired Energy Limiting Design for transition zones, which was shown to reduce uneven settlement effectively. In Ref. [12], transition zones are designed based on multi-objective optimization to minimize dynamic responses.

For settlement monitoring, the digital image correlation technique [13,14] is commonly used to measure settlements along the transition zone. Uneven subgrade settlement can induce bending deformation in the rail, commonly quantified by its bending angle (θ_s), as shown in Fig. 1. Mishra et al. [13] used the in-situ measured data to quantify the proportion of settlement to each layer of the transition zone and predicted the associated bending angle. Wang et al. [14] advanced settlement monitoring by integrating the interferometric synthetic aperture radar technique with the digital image correlation technique to capture both the magnitude and rate of differential settlement in the transition zone. Their measurement systems, mounted on a full-scale test vehicle, enabled real-time tracking of dynamic responses and track geometry quality in transition zones.

To implement effective measures to control uneven settlement in railway transition zones, it is crucial to understand the mechanisms of settlement initiation and development. Numerous empirical models have been proposed to predict settlement under cyclic loading, based on extensive experiments and field monitoring data. These models typically account for key factors such as dynamic stress distribution, subgrade stiffness degradation, and cumulative plastic deformation critical for analyzing the long-term performance of track-substructure systems under repeated train loads. Prominent examples include the models proposed by Sato [15], Okabe [16], Shenton [17], Monismith [18], Stewart [19], Li and Selig [20], and Bian [21].

However, a common difficulty in applying these models to transition zones lies in the requirement for predefined time-varying stress histories in the subgrade, rather than the constant stress amplitudes typically used in the experiments that underpin the empirical models. In reality, subgrade stresses vary significantly over time, driven by the dynamic wheel-rail forces as trains pass through settlement-affected zones. To overcome this limitation, several studies have integrated empirical settlement models into train-track dynamic interaction models to predict the permanent settlement considering dynamic wheel-rail forces which result in time-varying stress in the subgrade. Among these, Sato's model and Li-Selig's model are most commonly adopted. For ballasted tracks, Sato's model is commonly used due to its capacity to predict ballast settlement. Nielsen [22,23] developed a dynamic Train-Track-Transition Zone (TTTZ) model to predict the permanent settlement where an iterative method was employed to update track geometry degradation. Grossoni et al [24] conducted a semi-analytical study on the dynamic behavior of vehicle-track interaction to estimate track support system settlement. Nevertheless, these models exhibit deficiencies in adequately addressing the complex and nonlinear contact behavior between sleepers and ballast. Wang and Markine [9,25] establish a detailed finite element model of the transition zone to consider the nonlinearity of the sleeper-ballast contact.

While Sato's model is applied for ballast settlement prediction, ballastless track systems primarily experience settlement due to

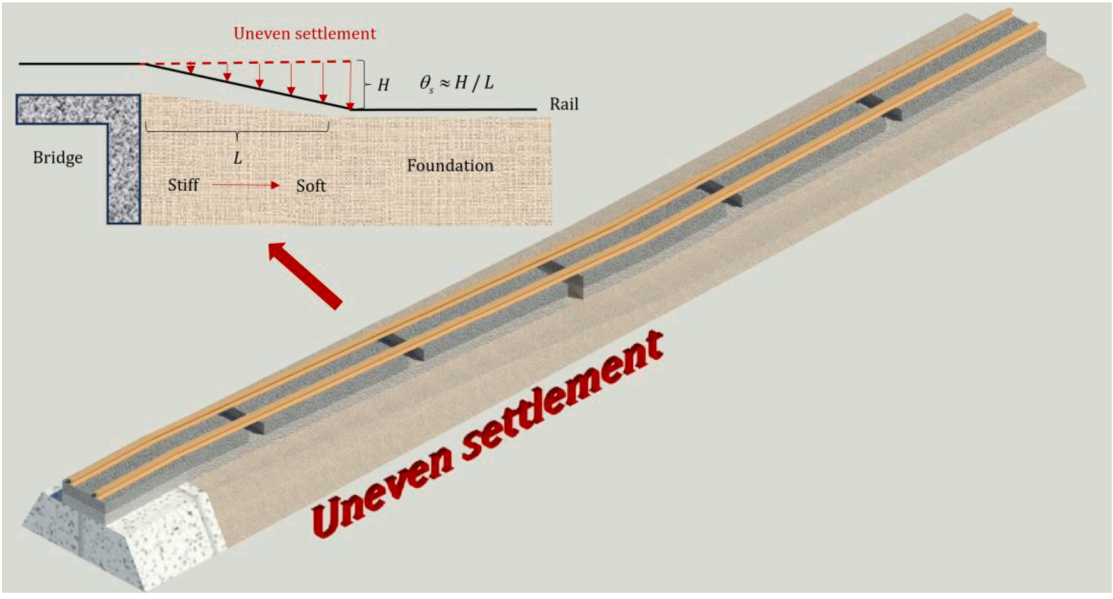

Fig. 1. The bending angle settlement in a transition zone.

deformation in the subgrade and underlying soil layers. Given its focus on predicting soil settlement under cyclic loading conditions, Li-Selig's model demonstrates higher applicability in the analysis of settlement in ballastless tracks. For example, Shan et al. [26] implemented it into a vehicle-track dynamic model for the prediction of CSTZ (Cumulative settlement of transition zone). Charoenwong et al [27] utilized a frequency-wavenumber technique to simulate the vibration of the ballastless track-subgrade system and further predicted subgrade settlement under cyclic trains using Li-Selig's model. Given the high stiffness contrast between ballastless track structures and underlying soil, interface detachment (void formation) may occur, leading to discrepancies between actual rail deformation and subgrade settlement. Consequently, rail irregularities induced by the settlement cannot be directly equated with the settlement profile itself. Although such detachment phenomena have been extensively studied in the sleeper void analysis of the ballasted track[25], there exist a few works related to ballastless track settlement that considered the detachment issue [26,27]. Hence, to depict the excitations of the train-track system more properly, a reliable long-term settlement prediction model must be able to consider potential detachment at the track-soil interface during the settlement process to obtain a more realistic mapped deformation (irregularity) of the rail.

Settlement acts as a strong excitation to the wheel-rail system, especially when its longitudinal wavelength is relatively small [28]. The settlement poses a risk to train running safety and amplifies vibrations in the track system remarkably [29]. While vertical contact models such as the Hertzian contact model are frequently used in settlement prediction [9,12,22,26,30], a more precise description of wheel-rail spatial contact geometries contributes to the assessment of train running states, such as the running stability [31,32], running safety [33,34], and potential derailment phenomenon [35,36] due to progressive settlement. However, the current literature lacks models that incorporate full three-dimensional wheel-rail contact to investigate settlement-induced train–track behavior, presenting a notable research gap.

Differential subgrade settlement is one of the crucial causes of track geometry degradation because it forms additional track irregularities and even causes local unsupported areas at track- subgrade interface [37]. While various studies have explored the shape, wavelength, and amplitude of train-induced settlements, accurately identifying the location of severe settlements is critically important for maintenance and management. Current approaches for identifying such areas rely on vehicle responses analyzed via machine learning [38], deep learning methods [39,40], or conventional time-frequency methods [41]. However, those methods rely on the relationship between vehicle responses and excitations (track irregularities), which requires relatively ideal conditions such as the wheel-rail keeping in contact which may not always be the case. Directly extracting the settlement components from the track irregularity data is difficult unless the sample size of settlement signals for data training/processing is large enough so that they can be treated in the frequency spectrum. When it comes to the identification of severe settlements, especially in the case of a small data sample size, only the high-resolution time-frequency method is efficient. To date, there is no literature to give a specific scheme or method to process severe settlement identification under the small sample size cases.

From the above review, three major gaps are identified in current CSTZ prediction studies using dynamic models:

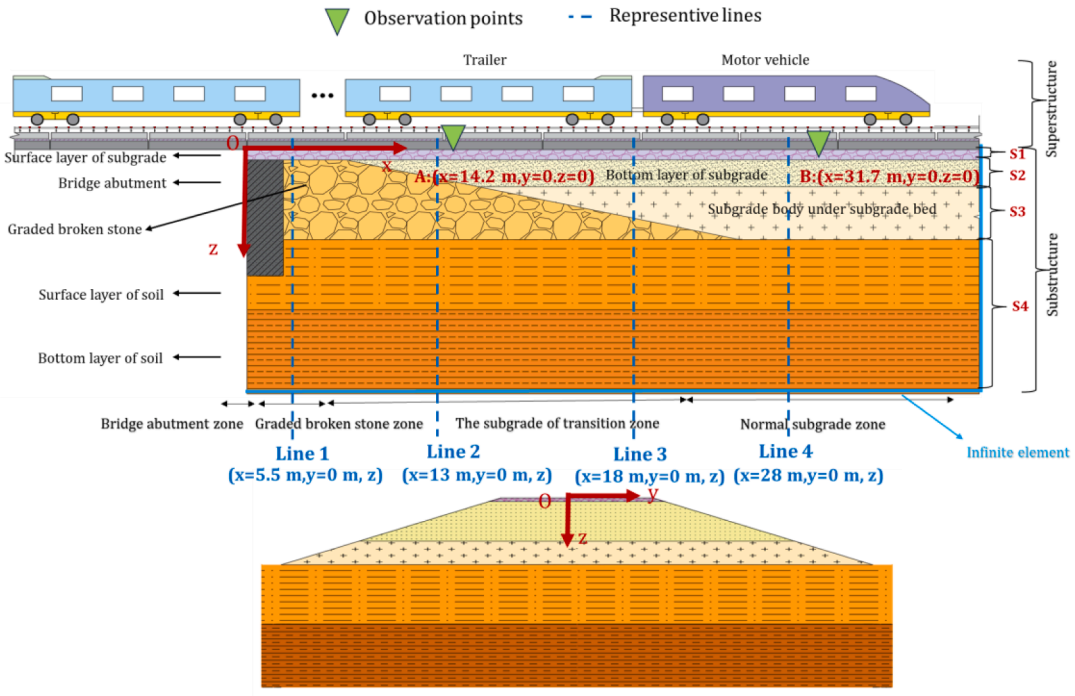

Fig. 2. Schematic diagram of the TTTZ system.

(1) Settlement–induced track irregularities cannot be directly equated with subgrade settlement, especially in ballastless tracks; the detachment of the track–soil interface must be considered to correctly determine rail deformation.
(2) A three-dimensional wheel-rail contact model should be considered in the simulation to analyze the behavior of the train-track system more properly, especially the running stability and safety due to settlements.
(3) Severe settlement localization needs to be addressed using effective methods capable of operating with limited data to support infrastructure maintenance and risk management.

To bridge these gaps, this paper proposes an integrated simulation framework that couples a dynamic train-track-transition zone model with a long-term subgrade settlement prediction model to analyze the train-induced settlement in the HSR transition zone. All the evolution processes of settlement are achieved by a stepwise method known as the "jump step" method [22,26,42,43]. The main contributions are as follows: (1) an iterative algorithm is introduced to update the track deformation under the evolutionary settlement; (2) the area with the severe settlement is identified according to the wavelength characteristics of settlement based on an effective time-frequency method.

This work is organized as follows. In Section 2, the formulation, solution, and validation of the dynamic train-track-transition zone model are presented; In Section 3, the settlement prediction model is elaborated; In Section 4, an iterative framework is presented to build the interaction between the dynamic train-track-transition zone model and the settlement prediction model in Sections 2 and 3 for long-term train-induced settlement prediction in transition zone; In Section 5, numerical examples are conducted to validate and illustrate the feasibility of the proposed framework. A novel time-frequency method based on the wavelet transform and short-time energy is proposed to identify the severe settlement area. In Section 6, key conclusions are drawn.

2. Modelling of train-track-transition zone interaction

This study establishes an integrated model for analyzing the dynamic behaviors of the TTTZ coupled system using the energy variation principle. As presented in Fig. 2, the present model consists of a high-speed train subsystem, ballastless track subsystem, and transition zone subsystem together with their interactions. Besides, the time-varying nature of the wheel-rail contact is explicitly incorporated into the wheel-rail interaction module. The modeling methodology and principles are described in Subsection 2.2, where a representative example is used to demonstrate the generation of dynamic matrices for the suspension system. For clarity and conciseness, the model formulation and numerical solution are organized into two dedicated algorithms. Validations are conducted by comparing the numerical results with results from literature and measured data. The system parameters of the TTTZ coupled dynamic model are listed in Appendix. A.

Two observation points are set, see Fig. 2. These points are respectively located at $(14.2\mathrm{m}, 0\mathrm{m}, 0\mathrm{m})$ and $(31.7\mathrm{m}, 0\mathrm{m}, 0\mathrm{m})$ for distinguishing the settlement difference between the transition zone and normal subgrade section, as discussed in Subsection 5.2. Analogously, four vertical representative lines located on four different cross-sections are set for studying the plastic strain distribution in Subsection 5.2, here we define them in advance.

These sections and monitoring locations are designed to capture the varying performance responses of the subgrade under dynamic train loading, thereby enabling a more nuanced understanding of their geotechnical characteristics and mechanical behaviour from a soil mechanics perspective.

2.1. Basic assumptions

The modelling of the TTTZ interaction follows the considerations and assumptions below:

(1) The vertical vibrations of the rail, the slab, and the baseplate are respectively simulated by the Bernoulli-Euler beam, Mindlin plate, and double-beam element, which are sufficient to reflect the motions of the track system as justified in [44]. Accordingly, the lateral vibrations of the rail are modelled by Euler beam elements. The 8-node solid elements are used to simulate the soil as a continuum.
(2) The track structures are assumed to be intact without any damage.
(3) The physical and mechanical parameters of subgrade and subsoil are homogeneous in each layer.
(4) The Hertzian contact theory and the Kalker creep theory are employed to simulate the normal and tangential contact between the wheel and rail.

2.2. Basic modelling methodology

As a time-varying system, the dynamic equation of motion of the TTTZ interaction system can be formulated in a matrix form [44], as follows :

$$\begin{bmatrix} \mathbf{M}_{VV} & \mathbf{0} & \mathbf{0} \\ \mathbf{0} & \mathbf{M}_{TT} & \mathbf{0} \\ \mathbf{0} & \mathbf{0} & \mathbf{M}_{ZZ} \end{bmatrix} \begin{Bmatrix} \ddot{\mathbf{X}}_V \\ \ddot{\mathbf{X}}_T \\ \ddot{\mathbf{X}}_Z \end{Bmatrix} + \begin{bmatrix} \mathbf{C}_{VV} & \mathbf{C}_{VT} & \mathbf{0} \\ \mathbf{C}_{TV} & \mathbf{C}_{TT} & \mathbf{C}_{TZ} \\ \mathbf{0} & \mathbf{C}_{ZT} & \mathbf{C}_{ZZ} \end{bmatrix} \begin{Bmatrix} \dot{\mathbf{X}}_V \\ \dot{\mathbf{X}}_T \\ \dot{\mathbf{X}}_Z \end{Bmatrix} + \begin{bmatrix} \mathbf{K}_{VV} & \mathbf{K}_{VT} & \mathbf{0} \\ \mathbf{K}_{TV} & \mathbf{K}_{TT} & \mathbf{K}_{TZ} \\ \mathbf{0} & \mathbf{K}_{ZT} & \mathbf{K}_{ZZ} \end{bmatrix} \begin{Bmatrix} \mathbf{X}_V \\ \mathbf{X}_T \\ \mathbf{X}_Z \end{Bmatrix} = \begin{Bmatrix} \mathbf{G}_V + \mathbf{F}_V \\ \mathbf{F}_T \\ \mathbf{0} \end{Bmatrix} \tag{2}$$

where**K**, **C**, **M** represent the stiffness, damping, and mass matrices, respectively; **X**, $\dot{\mathbf{X}}$ and $\ddot{\mathbf{X}}$ are the displacement, velocity, and acceleration vectors, respectively; the subscripts "*V*", "T", and "*Z*" denote the train, track, and substructure, respectively; $\mathbf{F}_{\mathrm{V}}$ and $\mathbf{F}_{\mathrm{T}}$ are the time-varying excitations generated by wheel-rail contact and track irregularities; $\mathbf{G}_{\mathrm{V}}$ denotes the static self-weight of the train.

The energy variation principle is introduced to generate the sub-matrices and force vectors in Eq. (2). For example, the stiffness matrix of the primary suspension of the vehicle (Fig. 3) can be derived by

$$\begin{cases} \delta\Pi = \sum_i \dfrac{\partial \Pi}{\partial C_{\mathrm{i}}} \delta C_{\mathrm{i}} = 0 \\ \Pi = \Pi_e + \Pi_p \end{cases} \tag{3}$$

where C_{i} is the independent DOF; Π is the total energy of the primary suspension system with Π_{e} the elastic potential energy and Π_p the negative value of work done by the external force. Π_{e} can be calculated by

$$\begin{cases} \Pi_e = \dfrac{1}{2} k_{p,z} (\Delta w)^2 \\ \Delta w = x_b - x_{w,i} \end{cases} \tag{4}$$

where Δw denotes the compressed value of the suspension spring whereas $k_{p,z}$ is the stiffness of the suspension spring; x_b and $x_{w,1\sim4}$ are the vertical displacements of the bogie and its four wheelsets.

By substitution of Eq. (4) into Eq. (3), one can obtain

$$\mathbf{K}_{p,z} = k_{p,z} (\mathbf{N}_w \otimes \mathbf{N}_w) \tag{5}$$

where $\mathbf{K}_{p,z}$ is the stiffness matrix of the primary suspension system for vertical direction; $\mathbf{N}_w$ is the shape function describing the compression of the suspension spring, given by [30]

$$\mathbf{N}_w = \begin{bmatrix} 1 & \dfrac{H_b}{2} & -1 \end{bmatrix}^{\mathrm{T}} \tag{6}$$

where H_b is the distance between two wheelsets under a bogie.

To improve simulation precision, a three-dimensional TTTZ dynamic model is employed. Generally, each subsystem can be modelled by the methodology organized in the following algorithm:

In this algorithm, the interactions between different components (track slab and baseplate, baseplate and subgrade soil) in the track-subgrade system are simulated by distributed springs and dampers. As a multi-scale system, the different components (taking the track slab and baseplate interface as an example) have different local coordinates $x-o-y$ and $\widetilde{x}-o-\widetilde{y}$ due to differences in mesh size, as shown in Fig. 4. Each element requires a different coordinate transformation to ensure consistency and compatibility of contact at the interface.

Here we take the vertical coupling stiffness matrix $\widehat{\mathbf{K}}_{bs}$ of the slab-baseplate interaction as an example to describe this coupling method as shown in Fig. 4. It should be noted that $\widehat{\mathbf{K}}_{bs}$ is a sub-matrix of $\widehat{\mathbf{K}}_{\mathrm{TT}}$ in Algorithm. 1. In addition, $\widehat{\mathbf{K}}_{\mathrm{TT}}$ also includes the coupling stiffness matrix of rail-slab interaction and part of the coupling stiffness matrix of baseplate-transition zone interaction, they can be found in Ref. [45].

Using a mapping transformation, we can establish a relation between the coordinate systems $x-o-y$ and $\widetilde{x}-o-\widetilde{y}$ respectively defined in slab element and baseplate element (see Fig. 4):

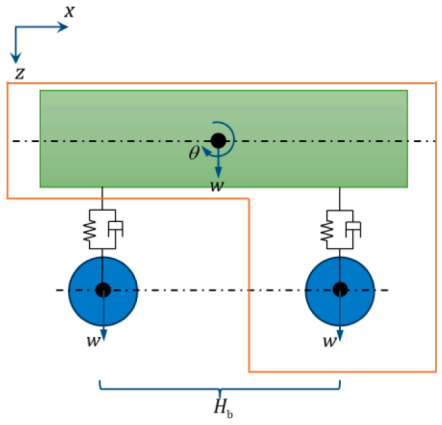

Fig. 3. Schematic diagram of the primary suspension system.

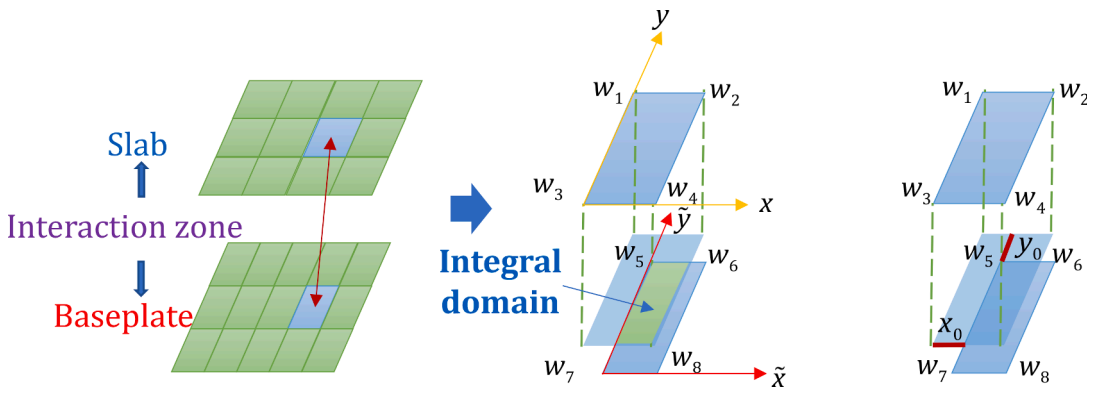

Fig. 4. Schematic diagram of the multi-scale coupling method.

$$\begin{cases} \tilde{x} = x + x_0 \\ \tilde{y} = y + y_0 \end{cases} \tag{7a}$$

Subsequently, the coupling stiffness matrix for the slab and baseplate elements can be generated by integral for the overlapping region in Fig. 4:

$$\widehat{\mathbf{K}}_{sb}^{\mathrm{e}} = k_{sb} \int_0^{L_x} \int_0^{L_y} [\mathbf{N}_{sb}(x, y, \tilde{x}, \tilde{y})]^{\mathrm{T}} [\mathbf{N}_{sb}(x, y, \tilde{x}, \tilde{y})] \mathrm{dxdy} \tag{7b}$$

with

$$\begin{cases} \mathbf{N}_{sb}(x, y, \tilde{x}, \tilde{y}) = [\,\mathbf{N}_s(x, y) \quad -\mathbf{N}_b(\tilde{x}, \tilde{y})\,] \\ \mathbf{N}_s(x, y) = [\,\mathrm{N}_{w1}(x, y) \quad \mathrm{N}_{w2}(x, y) \quad \mathrm{N}_{w3}(x, y) \quad \mathrm{N}_{w4}(x, y) \quad 0 \quad 0 \quad 0 \quad 0\,], \\ \mathbf{N}_b(\tilde{x}, \tilde{y}) = [\,0 \quad 0 \quad 0 \quad 0 \quad \mathrm{N}_{w5}(\tilde{x}, \tilde{y}) \quad \mathrm{N}_{w6}(\tilde{x}, \tilde{y}) \quad \mathrm{N}_{w7}(\tilde{x}, \tilde{y}) \quad \mathrm{N}_{w8}(\tilde{x}, \tilde{y})\,] \end{cases}$$

where $w1$, $w2$, $w3$,…, $w8$ denote the DOFs for vertical motion of the slab and baseplate elements, as shown in Fig. 4; $\widehat{\mathbf{K}}_{sb}^{\mathrm{e}}$ represents the elemental stiffness matrix of slab-baseplate interaction which should be assembled into $\widehat{\mathbf{K}}_{sb}$; $s$and b denote slab and baseplate; L_x and L_y represent the lengths of the slab element in x-axis and y-axis directions, respectively;$\mathbf{N}_s$ and $\mathbf{N}_b$ denote the shape functions of the slab and baseplate, as defined in Ref. [48]; k_{sb} denotes stiffness per area of the coupling spring of the slab-baseplate interaction which represents the filling layer between the slab and the baseplate.

The train is modeled as a multi-rigid-body system including one car body, two bogie frames, and four wheelsets The connections between them are stimulated as spring-dashpot elements, as shown in Fig. 5. For the car body and bogie frame, there are 5 DOFs for each component including motion of the transverse y_c and y_b, bounce z_c and z_b, yaw ψ_c and ψ_b, pitch β_c and β_b, rolling φ_c and φ_b; where the subscripts b and c represent the car body and bogie frame, respectively; there are 4 DOFs for wheelsets, including z_w, y_w, φ_w andψ_w; where the subscripts w denotes the wheelset; The contact between wheel and rail is simulated by nonlinear springs. The whole framework is shown in Fig. 5.

2.3. Solution procedure of the TTTZ interaction

The TTTZ system is a dynamic system with a large number of DOFs with nonlinear wheel-rail contact behavior. Therefore, solving Eq. (2) is time-consuming. In this study, an efficient solution algorithm is performed to improve the computational efficiency. Firstly, we divide the dynamic model into two sub-systems, i.e., the train-track sub-system and the transition zone sub-system. Secondly, setting the time sequences $\mathbf{T}_{\mathbb{R}} = (0, \Delta t_{\mathbb{R}}, 2\Delta t_{\mathbb{R}}, \ldots)$ and $\mathbf{T}_{\mathbb{Z}} = (0, \Delta t_{\mathbb{Z}}, 2\Delta t_{\mathbb{Z}}, \ldots)$ to depict the time instants of the train-track sub-system and transition zone system, respectively. Finally, the dynamic equations of motion of the two sub-systems are solved separately, and the equilibrium of the two sub-systems is maintained by the Newton-Raphson iterative method.

Assuming the multi-time-step ratio is $N_{TM} = \Delta t_{\mathbb{Z}} / \Delta t_{\mathbb{R}}$. When the time marching procedure goes to a condition $\mathbf{T} = \mathbf{T}_{\mathbb{Z}} = lN_{TM}\Delta t_{\mathbb{R}}, l = 0, 1, 2, \ldots, N$, namely the time marching of the transition zone sub-system and the train-track sub-system are equal, the two sub-systems should be solved simultaneously while the converged results can be obtained by the N-RIM. The entire solution procedure of the multi-time-step method can be organized as an Algorithm. 2.

The time used for solving the motion equations of the TTTZ interaction system is recorded to show the computational efficiency of the proposed algorithm. The present TTTZ dynamic model has 729106 DOFs including vehicle, track, and transition zone. Four cases are set for the analysis, namely $C_i = \Delta t_{\mathbb{Z}} / \Delta t_{\mathbb{R}}$, where i=1, 2, 4 6 to represent $\Delta t_{\mathbb{Z}} / \Delta t_{\mathbb{R}}$=1, 2, 4, and 6. The train speed considered in the simulation is 300 km/h.

When $\Delta t_{\mathbb{Z}} / \Delta t_{\mathbb{R}} = 1$, the algorithm degenerates to the solution with identical time step size, it costs approximately 2.99 h for 0.1 s

Algorithm 1

. xx.

i. Modelling the decoupled train-track-transition zone system based on Eqs. (3)-(6):

$$\begin{cases} \mathbf{M}_{VV}\ddot{\mathbf{X}}_V + \widetilde{\mathbf{C}}_{VV}\dot{\mathbf{X}}_V + \widetilde{\mathbf{K}}_{VV}\mathbf{X}_V = \mathbf{G}_V + \mathbf{F}_{VT} \\ \mathbf{M}_{TT}\ddot{\mathbf{X}}_T + \widetilde{\mathbf{C}}_{TT}\dot{\mathbf{X}}_T + \widetilde{\mathbf{K}}_{TT}\mathbf{X}_T = \mathbf{F}_{TV} + \mathbf{F}_{TZ} \\ \mathbf{M}_{ZZ}\ddot{\mathbf{X}}_Z + \widetilde{\mathbf{C}}_{ZZ}\dot{\mathbf{X}}_Z + \widetilde{\mathbf{K}}_{ZZ}\mathbf{X}_Z = \mathbf{F}_{ZT} \end{cases};$$

It should be noted that $\widetilde{\mathbf{M}}_{VV}$,$\widetilde{\mathbf{C}}_{VV}$,$\widetilde{\mathbf{K}}_{VV}$ respectively represent the damping and stiffness matrices of the train system without coupling parts, different to $\mathbf{C}_{VV}$,$\mathbf{K}_{VV}$ in Eq. (2). Similarly, $\widetilde{\mathbf{C}}_{TT}$,$\widetilde{\mathbf{K}}_{TT}$, $\widetilde{\mathbf{C}}_{ZZ}$ and $\widetilde{\mathbf{K}}_{ZZ}$respectively represent the damping and stiffness matrices of the track and substructure without coupling parts. $\mathbf{F}_{VT}$ and $\mathbf{F}_{TV}$ are the interaction forces between the train and track and they are equal in magnitude but opposite in direction. Analogously,$\mathbf{F}_{TZ}$ and $\mathbf{F}_{ZT}$ respectively represent the interaction forces between the track and transition zone, with equal magnitude and opposite direction. The train is simulated as a multi-rigid-body, and the specific configuration will be introduced in the following text. The track and transition zone are simulated by FEM, as described in Subsection 2.1.

ii. Modelling the interactions:

The above interaction forces $\mathbf{F}_{VT}$,$\mathbf{F}_{TV}$, $\mathbf{F}_{TZ}$and $\mathbf{F}_{ZT}$ are formulated as follows:

(i) Train-track interaction

The basic modeling approach of Vehicle-track dynamics theory [45] is adopted. That is, a wheel-rail spatial contact relation is considered by using the "*track line*" method [46]. The coupling of wheels and rails is implemented by

$$\begin{Bmatrix} \mathbf{F}_{VT} \\ \mathbf{F}_{TV} \end{Bmatrix} = \{\mathbf{F}_H\} + \{\mathbf{F}_C\}$$

where $\mathbf{F}_H$ denotes the normal Hertzian contact forces, $\mathbf{F}_C$ denotes the tangent creep forces, and they can be rewritten as an equation in matrix form. Taking $\mathbf{F}_H$ as an instance, we have:

$$\mathbf{F}_H = \begin{Bmatrix} -\mathbf{H}^1_{w,i} & \mathbf{H}^1_{r,i} \end{Bmatrix}^T \sum_i k^1_{H,i}\left(x^1_{w,i} - x^1_{r,i} - z^1_{r,i}\right) + \begin{Bmatrix} -\mathbf{H}^2_{w,i} & \mathbf{H}^2_{r,i} \end{Bmatrix}^T \sum_i k^2_{H,i}\left(x^2_{w,i} - x^2_{r,i} - z^2_{r,i}\right);$$

with $x^1_{w,i} = \left[\mathbf{H}^1_{w,i}\right]^T \mathbf{X}_V$, $x^1_{r,i} = \mathbf{N}^1_{r,i}\left[\mathbf{H}^1_{r,i}\right]^T \mathbf{X}_T$, $x^2_{w,i} = \left[\mathbf{H}^2_{w,i}\right]^T \mathbf{X}_V$, $x^2_{r,i} = \mathbf{N}^2_{r,i}\left[\mathbf{H}^2_{r,i}\right]^T \mathbf{X}_T$;

where the subscripts $i = 1 \sim 4$ denote the 1~4 wheelsets of the train, "r" and "w" represent the rail and wheelset, respectively; the superscripts "1" and "2" denote the left rail and right rail, respectively.$z^1_{r,i}$ and $z^2_{r,i}$ are the irregularities of the left rail and right rail, respectively; $\mathbf{H}^1_{w,i}$ and $\mathbf{H}^1_{r,i}$ denote the index matrices of excitations, which indicates the availability of excitations corresponding to any specific DOF in the left wheel-rail system; accordingly, $\mathbf{H}^2_{w,i}$ and $\mathbf{H}^2_{r,i}$ denote the index matrices corresponding to the right wheel-rail system, they can be found in [47]. $\mathbf{N}^1_{r,i}$ and $\mathbf{N}^2_{r,i}$ are the shape functions of the left rail and right rail, respectively.

The abovementioned expression of $\mathbf{F}_H$ can be rewritten as:

$$\mathbf{F}_H = \begin{Bmatrix} \mathbf{F}_{H,V} \\ \mathbf{F}_{H,T} \end{Bmatrix} - \begin{bmatrix} \overline{\mathbf{K}}_{VV} & \overline{\mathbf{K}}_{VT} \\ \overline{\mathbf{K}}_{TV} & \overline{\mathbf{K}}_{TT} \end{bmatrix} \begin{Bmatrix} \mathbf{X}_V \\ \mathbf{X}_T \end{Bmatrix}; \begin{cases} \overline{\mathbf{K}}_{VV} = \sum_i k^1_{H,i}\left[\mathbf{H}^1_{w,i}\right]\left[\mathbf{H}^1_{w,i}\right]^T + \sum_i k^2_{H,i}\left[\mathbf{H}^2_{w,i}\right]\left[\mathbf{H}^2_{w,i}\right]^T \\ \overline{\mathbf{K}}_{VT} = -\sum_i k^1_{H,i}\left[\mathbf{H}^1_{w,i}\right]\left[\mathbf{H}^1_{r,i}\mathbf{N}^1_{r,i}\right]^T - \sum_i k^2_{H,i}\left[\mathbf{H}^2_{w,i}\right]\left[\mathbf{H}^2_{r,i}\mathbf{N}^2_{r,i}\right]^T \\ \overline{\mathbf{K}}_{TV} = -\sum_i k^1_{H,i}\left[\mathbf{H}^1_{r,i}\mathbf{N}^1_{r,i}\right]\left[\mathbf{H}^1_{w,i}\right]^T - \sum_i k^2_{H,i}\left[\mathbf{H}^2_{r,i}\mathbf{N}^2_{r,i}\right]\left[\mathbf{H}^2_{w,i}\right]^T \\ \overline{\mathbf{K}}_{TT} = \sum_i k^1_{H,i}\left[\mathbf{H}^1_{r,i}\mathbf{N}^1_{r,i}\right]\left[\mathbf{H}^1_{r,i}\mathbf{N}^1_{r,i}\right]^T + \sum_i k^2_{H,i}\left[\mathbf{H}^2_{r,i}\mathbf{N}^2_{r,i}\right]\left[\mathbf{H}^2_{r,i}\mathbf{N}^2_{r,i}\right]^T \end{cases};$$

$$\{\mathbf{F}_{H,V} \quad \mathbf{F}_{H,T}\}^T = \sum_i z_{r,i}\left[\mathbf{H}^1_{w,i} \quad \mathbf{H}^1_{w,i}\right]\left[1 \quad -\mathbf{N}^1_{r,i}\right]^T + \sum_i y_{r,i}\left[\mathbf{H}^2_{w,i} \quad \mathbf{H}^2_{w,i}\right]\left[1 \quad -\mathbf{N}^2_{r,i}\right]^T$$

where $\mathbf{N}^1_{w,i}$ and $\mathbf{N}^1_{r,i}$ denote the shape function of the left wheel and left rail motions, respectively; $\mathbf{N}^2_{w,i}$ and $\mathbf{N}^2_{r,i}$ denote the shape function of the right wheel and right rail motions, respectively; $\overline{\mathbf{K}}$ denotes the interaction stiffness matrix of the wheel-rail system.

By using the same methodology, the creep forces can be assembled in a similar form so that we can establish the coupling matrix terms in Eq. (2), i.e.,

$$\begin{bmatrix} \mathbf{M}_{VV} & \mathbf{0} \\ \mathbf{0} & \mathbf{M}_{TT} \end{bmatrix} \begin{Bmatrix} \ddot{\mathbf{X}}_V \\ \ddot{\mathbf{X}}_T \end{Bmatrix} + \begin{bmatrix} \widetilde{\mathbf{C}}_{VV} + \overline{\mathbf{C}}_{VV} & \overline{\mathbf{C}}_{VT} \\ \overline{\mathbf{C}}_{TV} & \widetilde{\mathbf{C}}_{TT} + \overline{\mathbf{C}}_{TT} \end{bmatrix} \begin{Bmatrix} \dot{\mathbf{X}}_V \\ \dot{\mathbf{X}}_T \end{Bmatrix} + \begin{bmatrix} \widetilde{\mathbf{K}}_{VV} + \overline{\mathbf{K}}_{VV} & \overline{\mathbf{K}}_{VT} \\ \overline{\mathbf{K}}_{TV} & \widetilde{\mathbf{K}}_{TT} + \overline{\mathbf{K}}_{TT} \end{bmatrix} \begin{Bmatrix} \mathbf{X}_V \\ \mathbf{X}_T \end{Bmatrix} = \begin{Bmatrix} \mathbf{G}_V + \mathbf{F}_{H,V} + \mathbf{F}_{C,V} \\ \mathbf{F}_{H,T} + \mathbf{F}_{C,T} + \mathbf{F}_{TZ} \end{Bmatrix},$$

with $\begin{Bmatrix} \mathbf{F}_{H,V} + \mathbf{F}_{C,V} \\ \mathbf{F}_{H,T} + \mathbf{F}_{C,T} \end{Bmatrix} = \begin{Bmatrix} \mathbf{F}_V \\ \mathbf{F}_T \end{Bmatrix}$.

where $\overline{\mathbf{C}}$ denotes the interaction damping matrix of the wheel-rail system.

(ii) Track-transition zone interaction

Without loss of generality, the coupling of the track system and transition zone system follows the same principle:

$\begin{Bmatrix} \mathbf{F}_{TZ} \\ \mathbf{F}_{ZT} \end{Bmatrix} = -\begin{bmatrix} \widehat{\mathbf{K}}_{TT} & \widehat{\mathbf{K}}_{TZ} \\ \widehat{\mathbf{K}}_{ZT} & \widehat{\mathbf{K}}_{ZZ} \end{bmatrix} \begin{Bmatrix} \mathbf{X}_T \\ \mathbf{X}_Z \end{Bmatrix} - \begin{bmatrix} \widehat{\mathbf{C}}_{TT} & \widehat{\mathbf{C}}_{TZ} \\ \widehat{\mathbf{C}}_{ZT} & \widehat{\mathbf{C}}_{ZZ} \end{bmatrix} \begin{Bmatrix} \dot{\mathbf{X}}_T \\ \dot{\mathbf{X}}_Z \end{Bmatrix}$ is the matrix form of the interaction forces between the track and transition zone defined before, so that we have:

$$\begin{bmatrix} \mathbf{M}_{TT} & \mathbf{0} \\ \mathbf{0} & \mathbf{M}_{ZZ} \end{bmatrix} \begin{Bmatrix} \ddot{\mathbf{X}}_T \\ \ddot{\mathbf{X}}_Z \end{Bmatrix} + \begin{bmatrix} \widetilde{\mathbf{C}}_{TT} + \widehat{\mathbf{C}}_{TT} & \widehat{\mathbf{C}}_{TZ} \\ \widehat{\mathbf{C}}_{ZT} & \widetilde{\mathbf{C}}_{ZZ} + \widehat{\mathbf{C}}_{ZZ} \end{bmatrix} \begin{Bmatrix} \dot{\mathbf{X}}_T \\ \dot{\mathbf{X}}_Z \end{Bmatrix} + \begin{bmatrix} \widetilde{\mathbf{K}}_{TT} + \widehat{\mathbf{K}}_{TT} & \widehat{\mathbf{K}}_{TZ} \\ \widehat{\mathbf{K}}_{ZT} & \widetilde{\mathbf{K}}_{ZZ} + \widehat{\mathbf{K}}_{ZZ} \end{bmatrix} \begin{Bmatrix} \mathbf{X}_T \\ \mathbf{X}_Z \end{Bmatrix} = \begin{Bmatrix} \mathbf{F}_{H,T} + \mathbf{F}_{C,T} \\ \mathbf{0} \end{Bmatrix};$$

Notably, using the two dynamic equations of motion defined in **III.(i)** and **(ii)**, the expression of Eq. (2) can be assembled, and

$$\{\mathbf{G}_V + \mathbf{F}_V \quad \mathbf{F}_T \quad \mathbf{0}\}^T = \{\mathbf{G}_V + \mathbf{F}_{H,V} + \mathbf{F}_{C,V} \quad \mathbf{F}_{H,T} + \mathbf{F}_{C,T} \quad \mathbf{0}\}^T;$$

$$\begin{bmatrix} \mathbf{C}_{VV} & \mathbf{C}_{VT} & \mathbf{0} \\ \mathbf{C}_{TV} & \mathbf{C}_{TT} & \mathbf{C}_{TZ} \\ \mathbf{0} & \mathbf{C}_{ZT} & \mathbf{C}_{ZZ} \end{bmatrix} = \begin{bmatrix} \widetilde{\mathbf{C}}_{VV} + \overline{\mathbf{C}}_{VV} & \overline{\mathbf{C}}_{VT} & \mathbf{0} \\ \overline{\mathbf{C}}_{TV} & \widetilde{\mathbf{C}}_{TT} + \overline{\mathbf{C}}_{TT} + \widehat{\mathbf{C}}_{TT} & \widehat{\mathbf{C}}_{TZ} \\ \mathbf{0} & \widehat{\mathbf{C}}_{ZT} & \widetilde{\mathbf{C}}_{ZZ} + \widehat{\mathbf{C}}_{ZZ} \end{bmatrix};$$

$$\begin{bmatrix} \mathbf{K}_{VV} & \mathbf{K}_{VT} & \mathbf{0} \\ \mathbf{K}_{TV} & \mathbf{K}_{TT} & \mathbf{K}_{TZ} \\ \mathbf{0} & \mathbf{K}_{ZT} & \mathbf{K}_{ZZ} \end{bmatrix} = \begin{bmatrix} \widetilde{\mathbf{K}}_{VV} + \overline{\mathbf{K}}_{VV} & \overline{\mathbf{K}}_{VT} & \mathbf{0} \\ \overline{\mathbf{K}}_{TV} & \widetilde{\mathbf{K}}_{TT} + \overline{\mathbf{K}}_{TT} + \widehat{\mathbf{K}}_{TT} & \widehat{\mathbf{K}}_{TZ} \\ \mathbf{0} & \widehat{\mathbf{K}}_{ZT} & \widetilde{\mathbf{K}}_{ZZ} + \widehat{\mathbf{K}}_{ZZ} \end{bmatrix};$$

where $\widehat{\mathbf{K}}$ and $\widehat{\mathbf{C}}$ respectively denote the interaction stiffness and damping matrices of the track-transition zone system. At this point, the dynamic equation of motion of the TTTZ system expressed by Eq. (2) can be ultimately established.

(*continued on next page*)

Algorithm 1 (*continued*)

The coupling of the track and transition zone is implemented by using the ***multi-scale*** coupling method presented in [48], which is a versatile method to establish the coupling matrix between the elements with different mesh grids.

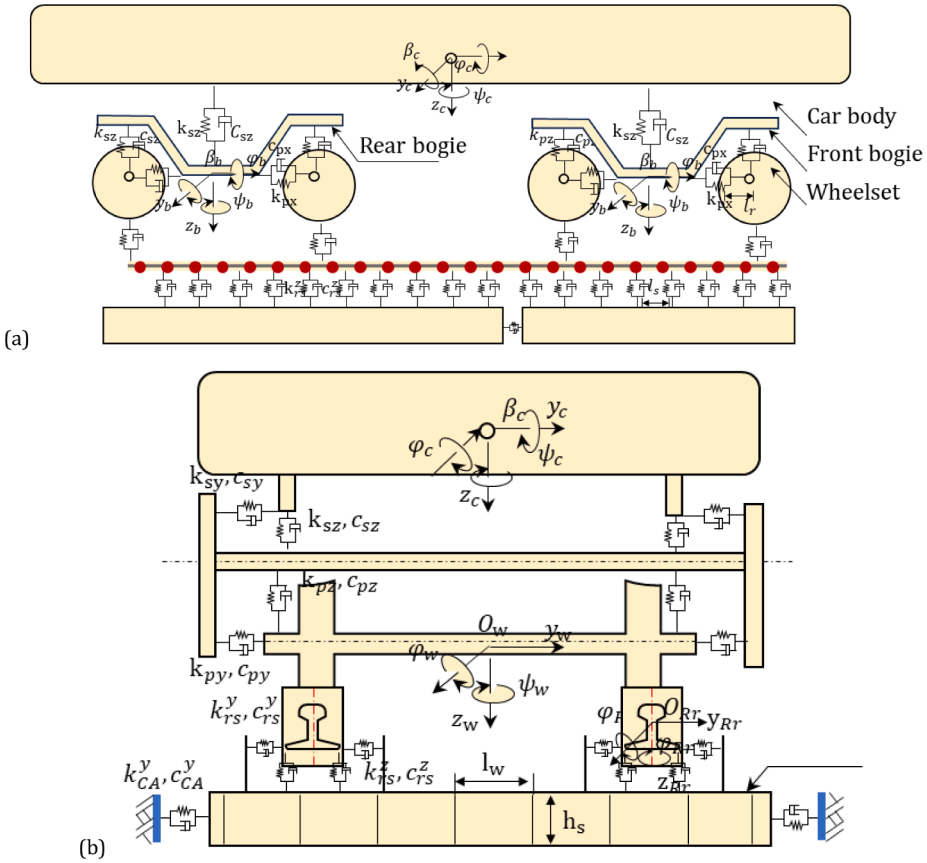

Fig. 5. Schematic diagram of the 3D train-track model (a side view; b end view).

analysis duration time and 30.18 h for 1.0 s analysis duration, as displayed in Table 1. The time costs for $\Delta t_{\mathbb{Z}}/\Delta t_{\mathbb{R}} = 2$, 4, and 6, and their proportion $\mathbb{Q}$ to $\Delta t_{\mathbb{Z}}/\Delta t_{\mathbb{R}} = 1$ case are also recorded. It can be seen that the $\Delta t_{\mathbb{Z}}/\Delta t_{\mathbb{R}} = 2$, 4, and 6 ($\Delta t_{\mathbb{R}}$=2.5×10^{-4} s) can save much time. When the multi-time-step size $\Delta t_{\mathbb{Z}}/\Delta t_{\mathbb{R}} = 6$ is adopted, the time spent is only 16.57% of the case $\Delta t_{\mathbb{Z}}/\Delta t_{\mathbb{R}} = 1$.

As for the convergence of the present model, we compared the results between $\Delta t_{\mathbb{Z}}/\Delta t_{\mathbb{R}} = 1$ case and $\Delta t_{\mathbb{Z}}/\Delta t_{\mathbb{R}} = 6$ case. Denoting solutions for identical time step case ($\Delta t_{\mathbb{Z}}/\Delta t_{\mathbb{R}} = 1$) and multi-time step size ($\Delta t_{\mathbb{Z}}/\Delta t_{\mathbb{R}} = 6$) of the two sub-systems as X_0 and X_1, then the difference between these two results can be calculated by $\mathrm{norm}(X_0 - X_1)/\mathrm{norm}(X_0)$. Fig. 6 shows the convergence of the error for rail displacement and slab displacement. It can be seen that after 5 iterations, the error will converge closely to 0.

It is proved that results converge at the time step $\Delta t_{\mathbb{R}}$=2.5×10^{-4} s as shown in Figs. 7 and 8. Assuming the results from the smallest time step size $\Delta t_{\mathbb{R}}$=2.5×10^{-6} s (denoted as $X_{2.5e^{-6}}$) approach the precise solution, the error of other cases can be estimated by $\mathrm{norm}(X_{2.5e^{-6}} - X_{\Delta t_{\mathbb{R}},i})/\mathrm{norm}(X_{2.5e^{-6}})$. It is clear from simulation results that the solutions from $\Delta t_{\mathbb{R}}$=2.5×10^{-4} s case are approximate to those of $\Delta t_{\mathbb{R}}$=2.5×10^{-6} s case, where the error of wheel-rail forces and rail displacement are only 0.21 % and 0.08 %, respectively.

2.4. Validation of the train-track-transition zone dynamic model

To validate the dynamic model in its effectiveness in predicting the vibration of railway tracks and soil, an in-situ measurement campaign was conducted in 2024 in a transition zone on the Beijing-Guangzhou HSR. The railway transition zone is in Changsha, Hunan Province, China. Fig. 9(a) shows the field situation. The ballastless track is CRTS III type, and the transition zone is from a bridge (abutment) to a subgrade. The high-precision wireless vibration sensors were mounted on the concrete track and soil to measure the vibration of the track and soil (Fig. 9(b)). The accelerometer for the track was mounted on the edge of the concrete base, and the accelerometer for the soil was mounted at the slope of the transition zone with 2.5 m depth (graded gravel). The recorded train speed was 300 km/h, and the train type was CRH2. Tables A.1 and A.2 display the train parameters used in this paper. The track and soil

Algorithm 2

. xxxx.

Initial Definition:

Subscript$\mathbb{R}$: the train-track sub-system; Subscript $\mathbb{Z}$: the transition zone sus-system;

$\boldsymbol{\Theta}$: the Newmark-β integration operator;

α: the factor for iteration convergence, which is $1e^{-7}$ in this study;

$\| * \|_2$: Euclidean norm of $*$;

$N_{TM} = \Delta t_{\mathbb{Z}} / \Delta t_{\mathbb{R}}$: the multi-time-step ratio.

i. Setting the initial computational parameters: the initial time sequence indexes$n_{\mathbb{R}} = 0$, $n_{\mathbb{Z}} = 0$;

ii. Implementing the time marching procedure:

For $t = 0 : \Delta t_{\mathbb{R}} : T_{\mathbb{R}}$(End)

If mod $(n_{\mathbb{Z}}, N_{TM}) = 0$, (note: this condition corresponds to the case that time marching of the transition zone sub-system and the train-track sub-system are equal. The transition zone sub-system and the train-track sub-system are solved simultaneously.)

(i) Solving the transition zone sub-system at the current time step $n_{\mathbb{Z}}$,:

$$\mathbf{F}^*_{\mathbb{Z},n_{\mathbb{Z}}\Delta t_{\mathbb{Z}}} = \mathbf{F}_{\mathbb{Z},n_{\mathbb{Z}}\Delta t_{\mathbb{Z}}} - \mathbf{K}_{\mathbb{Z}\mathbb{R}}\mathbf{X}_{\mathbb{R},(n_{\mathbb{Z}}-1)\Delta t_{\mathbb{Z}}} - \mathbf{C}_{\mathbb{Z}\mathbb{R}}\dot{\mathbf{X}}_{\mathbb{R},(n_{\mathbb{Z}}-1)\Delta t_{\mathbb{Z}}};$$

$$\left(\mathbf{X}_{\mathbb{Z},n_{\mathbb{Z}}\Delta t_{\mathbb{Z}}}, \dot{\mathbf{X}}_{\mathbb{Z},n_{\mathbb{Z}}\Delta t_{\mathbb{Z}}}, \ddot{\mathbf{X}}_{\mathbb{Z},n_{\mathbb{Z}}\Delta t_{\mathbb{Z}}}\right) = \boldsymbol{\Theta}\left(\mathbf{M}_{\mathbb{Z}\mathbb{Z}}, \mathbf{C}_{\mathbb{Z}\mathbb{Z}}, \mathbf{K}_{\mathbb{Z}\mathbb{Z}}, \mathbf{F}^*_{\mathbb{Z},n_{\mathbb{Z}}\Delta t_{\mathbb{Z}}}, \Delta t_{\mathbb{Z}}, \mathbf{X}_{\mathbb{Z},(n_{\mathbb{Z}}-1)\Delta t_{\mathbb{Z}}}, \dot{\mathbf{X}}_{\mathbb{Z},(n_{\mathbb{Z}}-1)\Delta t_{\mathbb{Z}}}, \ddot{\mathbf{X}}_{\mathbb{Z},(n_{\mathbb{Z}}-1)\Delta t_{\mathbb{Z}}}\right)$$

(ii) Solving the train-track sub-system at the current time step $n_{\mathbb{R}}$

$$\mathbf{F}^*_{\mathbb{R},n_{\mathbb{R}}\Delta t_{\mathbb{R}}} = \mathbf{F}_{\mathbb{R},n_{\mathbb{R}}\Delta t_{\mathbb{R}}} - \mathbf{K}_{\mathbb{R}\mathbb{Z}}\mathbf{X}_{\mathbb{Z},(n_{\mathbb{R}}-1)\Delta t_{\mathbb{R}}} - \mathbf{C}_{\mathbb{R}\mathbb{Z}}\dot{\mathbf{X}}_{\mathbb{Z},(n_{\mathbb{R}}-1)\Delta t_{\mathbb{R}}};$$

$$\left(\mathbf{X}_{\mathbb{R},n_{\mathbb{R}}\Delta t_{\mathbb{R}}}, \dot{\mathbf{X}}_{\mathbb{R},n_{\mathbb{R}}\Delta t_{\mathbb{R}}}, \ddot{\mathbf{X}}_{\mathbb{R},n_{\mathbb{R}}\Delta t_{\mathbb{R}}}\right) = \boldsymbol{\Theta}\left(\mathbf{M}_{\mathbb{R}\mathbb{R}}, \mathbf{C}_{\mathbb{R}\mathbb{R}}, \mathbf{K}_{\mathbb{R}\mathbb{R}}, \mathbf{F}^*_{\mathbb{R},n_{\mathbb{R}}\Delta t_{\mathbb{R}}}, \Delta t_{\mathbb{R}}, \mathbf{X}_{\mathbb{R},(n_{\mathbb{R}}-1)\Delta t_{\mathbb{R}}}, \dot{\mathbf{X}}_{\mathbb{R},(n_{\mathbb{R}}-1)\Delta t_{\mathbb{R}}}, \ddot{\mathbf{X}}_{\mathbb{R},(n_{\mathbb{R}}-1)\Delta t_{\mathbb{R}}}\right)$$

(iii) The N-RIM is applied to maintain the equilibrium of the forces between the two sub-systems:

(a) Storing the displacement vector of the train-track system.

$$\widetilde{\mathbf{X}}_{\mathbb{R},n_{\mathbb{Z}}\Delta t_{\mathbb{Z}}} = \mathbf{X}_{\mathbb{R},n_{\mathbb{Z}}\Delta t_{\mathbb{Z}}}$$

(b) Solving the transition zone sub-system using $\mathbf{X}_{\mathbb{R},n_{\mathbb{Z}}\Delta t_{\mathbb{Z}}}$ and $\dot{\mathbf{X}}_{\mathbb{R},n_{\mathbb{Z}}\Delta t_{\mathbb{Z}}}$:

$$\widetilde{\mathbf{F}}^*_{\mathbb{Z},n_{\mathbb{Z}}\Delta t_{\mathbb{Z}}} = \mathbf{F}_{\mathbb{Z},n_{\mathbb{Z}}\Delta t_{\mathbb{Z}}} - \mathbf{K}_{\mathbb{Z}\mathbb{R}}\mathbf{X}_{\mathbb{R},n_{\mathbb{Z}}\Delta t_{\mathbb{Z}}} - \mathbf{C}_{\mathbb{Z}\mathbb{R}}\dot{\mathbf{X}}_{\mathbb{R},n_{\mathbb{Z}}\Delta t_{\mathbb{Z}}};$$

$$\left(\widetilde{\mathbf{X}}_{\mathbb{Z},n_{\mathbb{Z}}\Delta t_{\mathbb{Z}}}, \widetilde{\dot{\mathbf{X}}}_{\mathbb{Z},n_{\mathbb{Z}}\Delta t_{\mathbb{Z}}}, \widetilde{\ddot{\mathbf{X}}}_{\mathbb{Z},n_{\mathbb{Z}}\Delta t_{\mathbb{Z}}}\right) = \boldsymbol{\Theta}\left(\mathbf{M}_{\mathbb{Z}\mathbb{Z}}, \mathbf{C}_{\mathbb{Z}\mathbb{Z}}, \mathbf{K}_{\mathbb{Z}\mathbb{Z}}, \widetilde{\mathbf{F}}^*_{\mathbb{Z},n_{\mathbb{Z}}\Delta t_{\mathbb{Z}}}, \Delta t_{\mathbb{Z}}, \mathbf{X}_{\mathbb{Z},(n_{\mathbb{Z}}-1)\Delta t_{\mathbb{Z}}}, \dot{\mathbf{X}}_{\mathbb{Z},(n_{\mathbb{Z}}-1)\Delta t_{\mathbb{Z}}}, \ddot{\mathbf{X}}_{\mathbb{Z},(n_{\mathbb{Z}}-1)\Delta t_{\mathbb{Z}}}\right)$$

(c) Solving the train-track system using $\widetilde{\mathbf{X}}_{\mathbb{Z},n_{\mathbb{Z}}\Delta t_{\mathbb{Z}}}$ and $\widetilde{\dot{\mathbf{X}}}_{\mathbb{Z},n_{\mathbb{Z}}\Delta t_{\mathbb{Z}}}$:

$$\widetilde{\mathbf{F}}^*_{\mathbb{R},n_{\mathbb{R}}\Delta t_{\mathbb{R}}} = \mathbf{F}_{\mathbb{R},n_{\mathbb{R}}\Delta t_{\mathbb{R}}} - \mathbf{K}_{\mathbb{R}\mathbb{Z}}\widetilde{\mathbf{X}}_{\mathbb{Z},n_{\mathbb{Z}}\Delta t_{\mathbb{Z}}} - \mathbf{C}_{\mathbb{R}\mathbb{Z}}\widetilde{\dot{\mathbf{X}}}_{\mathbb{Z},n_{\mathbb{Z}}\Delta t_{\mathbb{Z}}};$$

$$\left(\mathbf{X}_{\mathbb{R},n_{\mathbb{R}}\Delta t_{\mathbb{R}}}, \dot{\mathbf{X}}_{\mathbb{R},n_{\mathbb{R}}\Delta t_{\mathbb{R}}}, \ddot{\mathbf{X}}_{\mathbb{R},n_{\mathbb{R}}\Delta t_{\mathbb{R}}}\right) = \boldsymbol{\Theta}\left(\mathbf{M}_{\mathbb{R}\mathbb{R}}, \mathbf{C}_{\mathbb{R}\mathbb{R}}, \mathbf{K}_{\mathbb{R}\mathbb{R}}, \widetilde{\mathbf{F}}^*_{\mathbb{R},n_{\mathbb{R}}\Delta t_{\mathbb{R}}}, \Delta t_{\mathbb{R}}, \mathbf{X}_{\mathbb{R},(n_{\mathbb{R}}-1)\Delta t_{\mathbb{R}}}, \dot{\mathbf{X}}_{\mathbb{R},(n_{\mathbb{R}}-1)\Delta t_{\mathbb{R}}}, \ddot{\mathbf{X}}_{\mathbb{R},(n_{\mathbb{R}}-1)\Delta t_{\mathbb{R}}}\right)$$

(d) Repeating steps **(a)** to **(c)** until $\| \widetilde{\mathbf{X}}_{\mathbb{R},n_{\mathbb{Z}}\Delta t_{\mathbb{Z}}} - \mathbf{X}_{\mathbb{R},n_{\mathbb{Z}}\Delta t_{\mathbb{Z}}} \|_2 < \alpha$

(e) Updating the solution of the transition zone system

$$\left(\mathbf{X}_{\mathbb{Z},n_{\mathbb{Z}}\Delta t_{\mathbb{Z}}}, \dot{\mathbf{X}}_{\mathbb{Z},n_{\mathbb{Z}}\Delta t_{\mathbb{Z}}}, \ddot{\mathbf{X}}_{\mathbb{Z},n_{\mathbb{Z}}\Delta t_{\mathbb{Z}}}\right) = \left(\widetilde{\mathbf{X}}_{\mathbb{Z},n_{\mathbb{Z}}\Delta t_{\mathbb{Z}}}, \widetilde{\dot{\mathbf{X}}}_{\mathbb{Z},n_{\mathbb{Z}}\Delta t_{\mathbb{Z}}}, \widetilde{\ddot{\mathbf{X}}}_{\mathbb{Z},n_{\mathbb{Z}}\Delta t_{\mathbb{Z}}}\right)$$

(iv) Updating the parameters: $n_{\mathbb{R}} = n_{\mathbb{R}} + 1$, $n_{\mathbb{Z}} = n_{\mathbb{Z}} + 1$;

elseif mod $(n_{\mathbb{Z}}, N_{TM}) \neq 0$

(i) Calculating the solution of the transition zone system at the current time point by using the interpolation between $\left(\mathbf{X}_{\mathbb{Z},n_{\mathbb{Z}}\Delta t_{\mathbb{Z}}}, \dot{\mathbf{X}}_{\mathbb{Z},n_{\mathbb{Z}}\Delta t_{\mathbb{Z}}}, \ddot{\mathbf{X}}_{\mathbb{Z},n_{\mathbb{Z}}\Delta t_{\mathbb{Z}}}\right)$ and $\left(\mathbf{X}_{\mathbb{Z},(n_{\mathbb{Z}}-1)\Delta t_{\mathbb{Z}}}, \dot{\mathbf{X}}_{\mathbb{Z},(n_{\mathbb{Z}}-1)\Delta t_{\mathbb{Z}}}, \ddot{\mathbf{X}}_{\mathbb{Z},(n_{\mathbb{Z}}-1)\Delta t_{\mathbb{Z}}}\right)$, given by

$$\begin{cases} \mathbf{X}_{\mathbb{Z},n_{\mathbb{R}}\Delta t_{\mathbb{R}}} = \mathbf{X}_{\mathbb{Z},(n_{\mathbb{Z}}-1)\Delta t_{\mathbb{Z}}} + \left(\dfrac{\mathbf{X}_{\mathbb{Z},n_{\mathbb{Z}}\Delta t_{\mathbb{Z}}} - \mathbf{X}_{\mathbb{Z},(n_{\mathbb{Z}}-1)\Delta t_{\mathbb{Z}}}}{N_{T_{\mathbb{Z}}=T_{\mathbb{R}}}}\right) \bmod \left(\dfrac{n_{\mathbb{Z}}}{n_{\mathbb{R}}}, N_{T_{\mathbb{Z}}=T_{\mathbb{R}}}\right) \\ \dot{\mathbf{X}}_{\mathbb{Z},n_{\mathbb{R}}\Delta t_{\mathbb{R}}} = \dot{\mathbf{X}}_{\mathbb{Z},(n_{\mathbb{Z}}-1)\Delta t_{\mathbb{Z}}} + \left(\dfrac{\dot{\mathbf{X}}_{\mathbb{Z},n_{\mathbb{Z}}\Delta t_{\mathbb{Z}}} - \dot{\mathbf{X}}_{\mathbb{Z},(n_{\mathbb{Z}}-1)\Delta t_{\mathbb{Z}}}}{N_{T_{\mathbb{Z}}=T_{\mathbb{R}}}}\right) \bmod \left(\dfrac{n_{\mathbb{Z}}}{n_{\mathbb{R}}}, N_{T_{\mathbb{Z}}=T_{\mathbb{R}}}\right) \\ \ddot{\mathbf{X}}_{\mathbb{Z},n_{\mathbb{R}}\Delta t_{\mathbb{R}}} = \ddot{\mathbf{X}}_{\mathbb{Z},(n_{\mathbb{Z}}-1)\Delta t_{\mathbb{Z}}} + \left(\dfrac{\ddot{\mathbf{X}}_{\mathbb{Z},n_{\mathbb{Z}}\Delta t_{\mathbb{Z}}} - \ddot{\mathbf{X}}_{\mathbb{Z},(n_{\mathbb{Z}}-1)\Delta t_{\mathbb{Z}}}}{N_{T_{\mathbb{Z}}=T_{\mathbb{R}}}}\right) \bmod \left(\dfrac{n_{\mathbb{Z}}}{n_{\mathbb{R}}}, N_{T_{\mathbb{Z}}=T_{\mathbb{R}}}\right) \end{cases}$$

(ii) Solving the train-track system at the current time point

$$\mathbf{F}^*_{\mathbb{R},n_{\mathbb{R}}\Delta t_{\mathbb{R}}} = \mathbf{F}_{\mathbb{R},n_{\mathbb{R}}\Delta t_{\mathbb{R}}} - \mathbf{K}_{\mathbb{R}\mathbb{Z}}\mathbf{X}_{\mathbb{Z},n_{\mathbb{R}}\Delta t_{\mathbb{R}}} - \mathbf{C}_{\mathbb{R}\mathbb{Z}}\dot{\mathbf{X}}_{\mathbb{Z},n_{\mathbb{R}}\Delta t_{\mathbb{R}}};$$

$$\left(\mathbf{X}_{\mathbb{R}}, \dot{\mathbf{X}}_{\mathbb{R}}, \ddot{\mathbf{X}}_{\mathbb{R}}\right) = \boldsymbol{\Theta}\left(\mathbf{M}_{\mathbb{R}\mathbb{R}}, \mathbf{C}_{\mathbb{R}\mathbb{R}}, \mathbf{K}_{\mathbb{R}\mathbb{R}}, \mathbf{F}^*_{\mathbb{R}}, \Delta t_{\mathbb{R}}\right);$$

(iii) Updating the parameters: $n_{\mathbb{R}} = n_{\mathbb{R}} + 1$;

end

end

parameters are listed in Tables A.3 and A.4. The geometry of the track structure is shown in Fig. 10.

The comparisons between simulated and measured accelerations, as illustrated in Figs. 11 and 12 validate the effectiveness of the proposed dynamic model in accurately estimating the responses of the track and soil. Some fundamental characteristic frequencies f_1, f_2, f_3 determined by train speed and wheelset length can be observed in the frequency spectrum. The first characteristic frequency f_1 is determined by the train speed V=300 km/h and the distance between the 1st and 4th wheelsets L_1=20 m, i.e., $f_1 = \frac{V}{L_1}$, which is reported as a vital frequency induced by the train load characteristics [49,50] and can be explained as the coherence phenomenon [51]. Accordingly f_2 and f_3 are determined by $f_2 = \frac{V}{L_2}$ and $f_1 = \frac{V}{L_3}$ where L_2=17.5 m denotes the distance between the 2nd (1st) and 4th (3rd) wheelsets, L_3=15 m denotes the distance between the 2nd and 3rd wheelsets. It can be seen the integral multiple of f_1, f_2 and f_3 can be observed, which is attributed to the periodicity of the train load excitations. Moreover, some dominated frequencies occur in the lower

Table 1
Computation costs for the solution of the TTTZ model using the present algorithm.

Duration of analysis (s)	Duration of simulation (h)			
	C_1	$C_2/\mathbb{Q}$	$C_4/\mathbb{Q}$	$C_6/\mathbb{Q}$
0.1	2.99	1.49/50.00%	0.75/25.10%	0.50/16.74%
0.2	5.98	3.00/50.16%	1.5/25.08%	1.00/16.72%
0.3	8.98	4.50/50.10%	2.25/25.05%	1.50/16.70%
0.4	11.99	6.00/50.05%	3.00/25.03%	2.00/16.68%
0.5	15.01	7.50/50.00%	3.75/24.98%	2.50/16.65%
0.6	18.02	9.00/49.98%	4.51/25.01%	3.00/16.65%
0.7	21.03	10.51/49.97%	5.26/25.00%	3.50/16.65%
0.8	24.03	12.00/49.96%	6.01/24.99%	4.00/16.65%
0.9	27.04	13.51/49.97%	6.76/24.98%	4.50/16.64%
1.0	30.18	15.01/49.75%	7.51/24.90%	5.00/16.57%

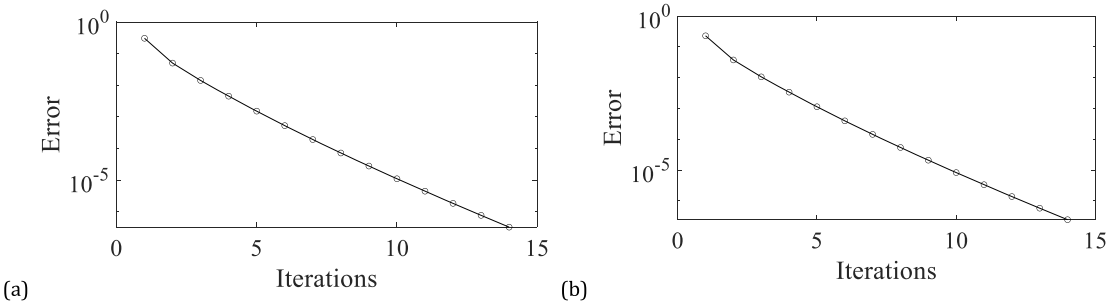

Fig. 6. Convergence of computational error of the algorithm in each iteration (a. rail displacement; b. slab displacement).

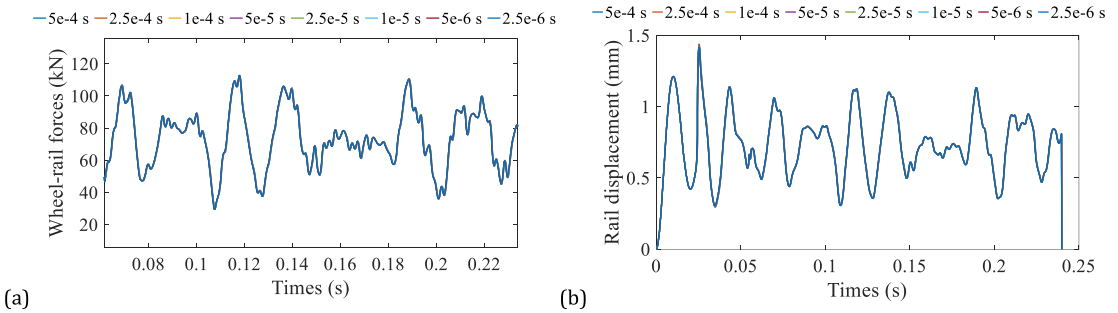

Fig. 7. Comparisons of different time step size cases (a. wheel-rail forces; b. rail displacements).

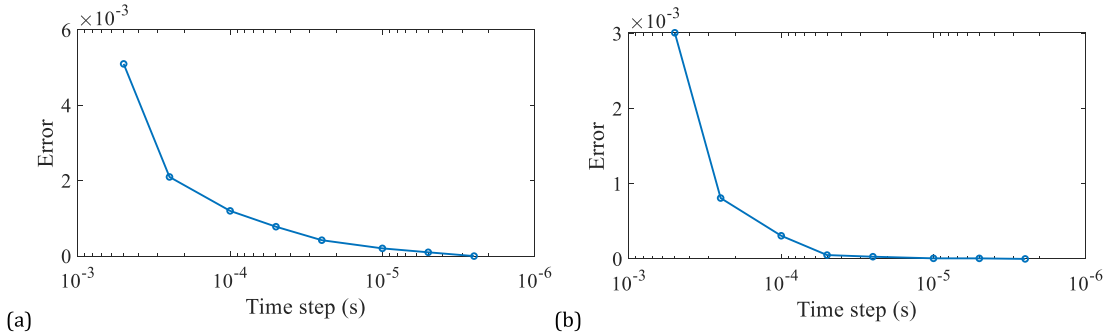

Fig. 8. Convergence of computational error of different time step size cases.

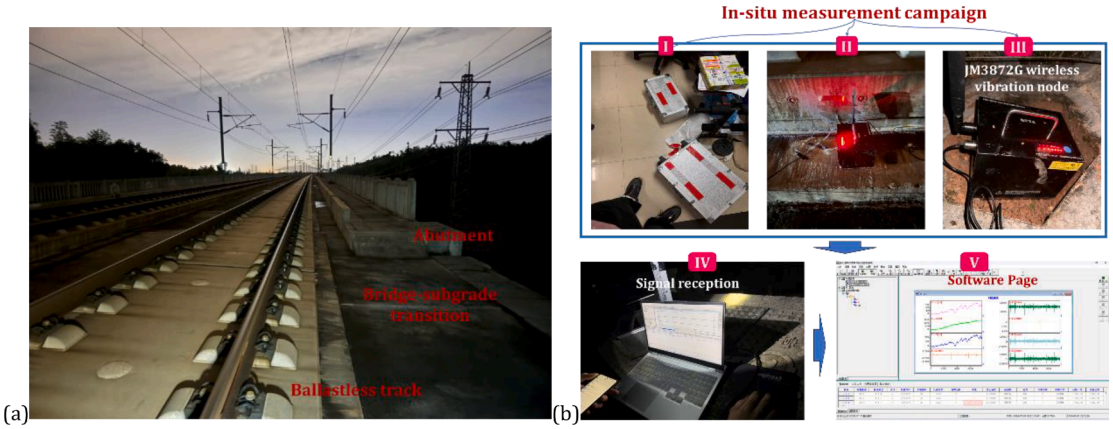

Fig. 9. The in-situ measurement campaign (a. in-situ measurement campaign about the bridge-subgrade transition zone in Changsha, Hunan province, China. Photo by Borong Peng and Zheng Li, Central South University, 4/3/2024, 2:21 am; b. measurement process).

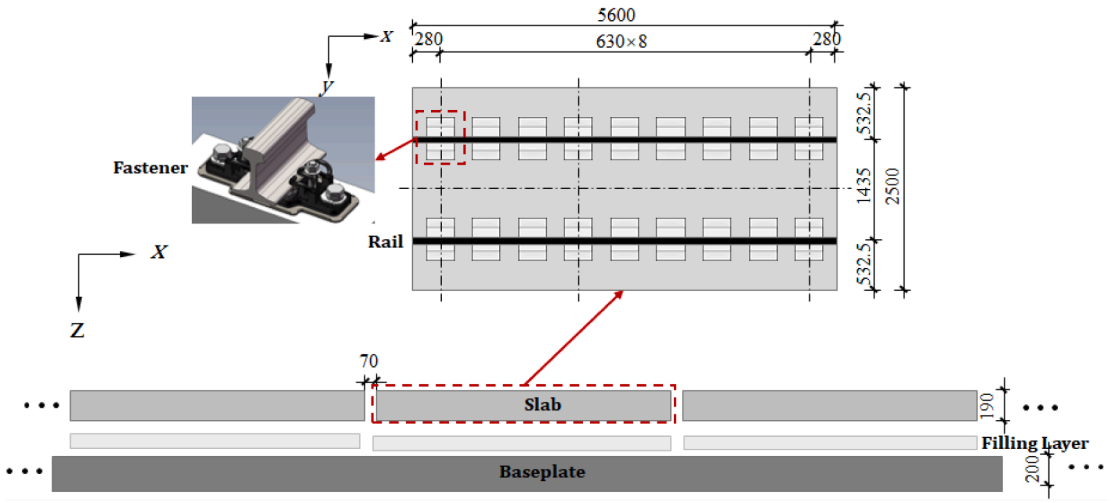

Fig. 10. CRTS III ballastless track used in China HSR.

frequency band, and they are induced by the distance between the wheelsets from different carriages, and are close to $0.5f_1$ and $0.5f_2$. The comparison illustrates the effectiveness of the simulation of this work.

3. Long-term settlement prediction for the transition zone

The TTTZ model presented and validated in previous section can be utilized to calculate the dynamic stress of soil induced by a passing train which is a short-term response. For long-term settlement prediction, a settlement prediction model is needed and integrated into the TTTZ. In this section, the settlement model to be used is described in detail. The settlement model should have the following requirements:

(1) The time-varying dynamic stresses from traffic load can be considered in the model;
(2) Describing the functional relationship between the dynamic stresses, the cycles of loads, and the plastic/permanent deformation;
(3) The cumulative progress of plastic deformation/strain can be described.

3.1. Basic assumptions

To meet the requirements mentioned above, we need to make the following assumptions:

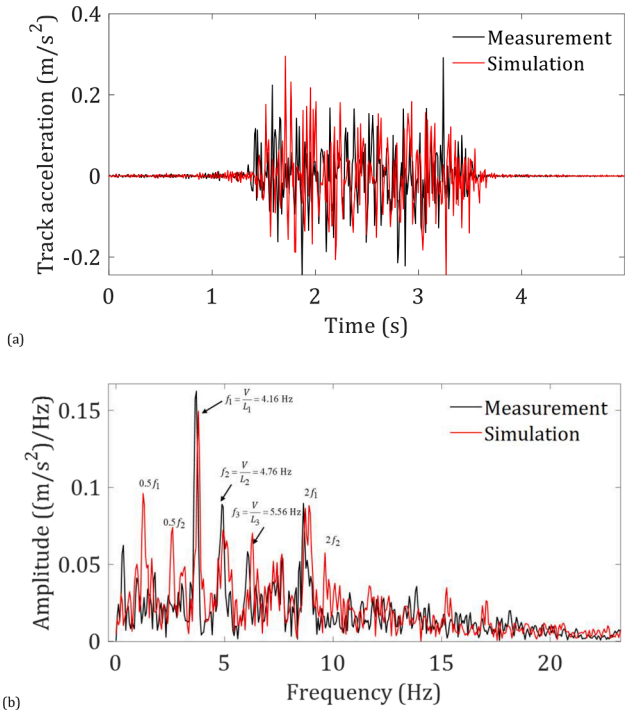

Fig. 11. Comparison of the track slab accelerations (a. time history; b. Fourier spectrum).

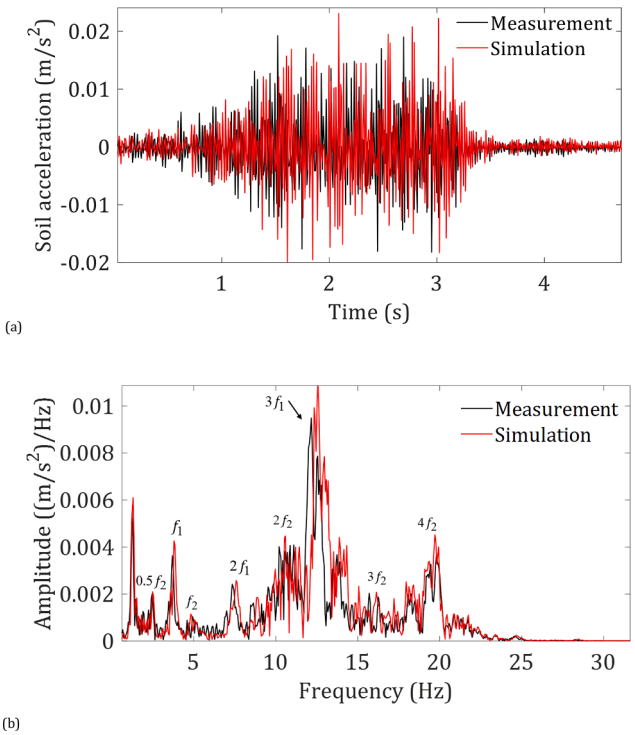

Fig. 12. Comparison of the soil accelerations (a. time history; b. Fourier spectrum).

(1) The impact load of high-speed trains is short-term; therefore, the migration of moisture in the soil cannot be considered.
(2) The constitutive model of soil does not change in simulation. That is, a linear soil model is used in Section 2 for improving simulation efficiency. Similarly, the soil of the transition zone is an isotropic material. The settlement model usually involves the computation of deviator stresses. Hence, the coupling of stresses from different directions is not time-efficient in simulation. The same assumption is also used in the literature about railway settlement [22,25].

3.2. Subgrade settlement model

As outlined in Section 1, numerous models have been developed to predict the permanent deformation or strain of railway ballast or subgrade materials. Among these, the majority are formulated as power-exponential equations involving the number of load cycles N_P and dynamic stress σ_d, such as the power-exponential model proposed by Li and Selig [20].

$$\widetilde{\varepsilon}(N_P) = a\left(\frac{\widetilde{\sigma}_d}{\widetilde{\sigma}_s}\right)^m (N_P)^b \tag{8}$$

where the parameters a, b and m need to be determined by calibration with experiments; $\widetilde{\sigma}_d$ is dynamic deviator stresses of materials and $\widetilde{\sigma}_s$ the static strength of the soil respectively; $\widetilde{\varepsilon}$ is the plastic strain obtained by this power exponential formula. Li-Selig's model assumes the occurrence of the plastic strain of geo-material is accumulated progress and will change with the variation of the magnitude of loads.

Additionally, other models exhibit similar mathematical formulations but are tailored for different geotechnical materials. Sato's model [15] is particularly practical, as it describes the relationship between the permanent deformation of ballasted tracks and the sleeper-ballast contact forces (refer to the work of Li and Nielsen [22] for details). For ballastless tracks with subgrade transition zones,

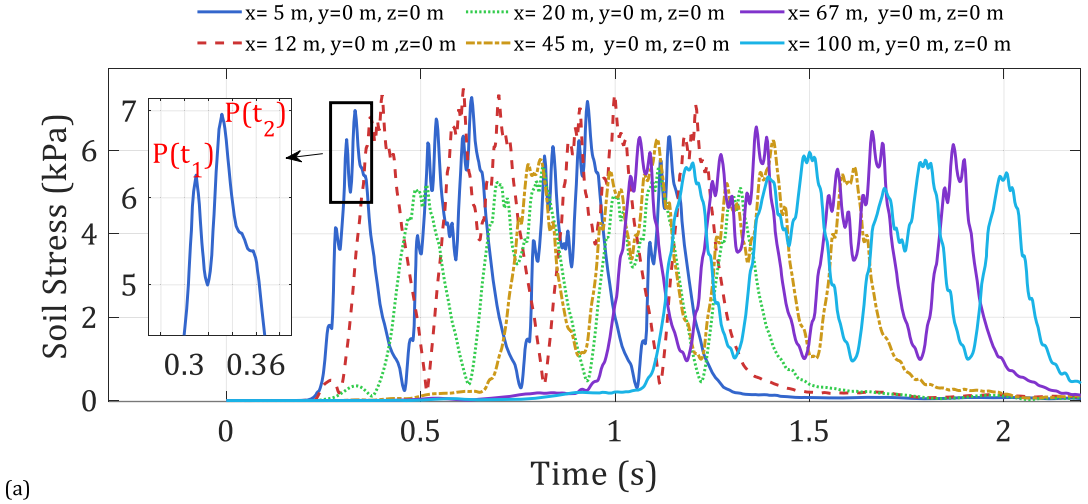

Fig. 13. Time history of dynamic deviator stresses (a. soil surface; b. 10 depth).

the Li-Selig model is more suitable due to its convenience, as it only requires the computation of deviatoric stresses.

3.3. Application of the settlement model in the TTTZ model

In the present study, Li-Selig's model is implemented, where the parameters a, b and m has been evaluated by Guo and Zhai [43]. The dynamic deviator stress $\widetilde{\sigma}_{\mathrm{d}}$ generated by high-speed train can be calculated by

$$\widetilde{\sigma}_d = \frac{\sqrt{(\sigma_{xx}-\sigma_{yy})^2+(\sigma_{xx}-\sigma_{zz})^2+(\sigma_{yy}-\sigma_{zz})^2+6(\tau_{xy}{}^2+\tau_{yz}{}^2+\tau_{xz}{}^2)}}{\sqrt{2}} \tag{9}$$

where $\sigma_{xx},\sigma_{yy},\sigma_{zz},\tau_{xy},\tau_{yz},\tau_{xz}$ are stresses with directionality. Note that the deviator stress $\widetilde{\sigma}_{\mathrm{d}}$ is scalar, that is, the direction problem of stress in the Li-Selig model is not considered. If the directional stresses are used, principal stress rotation should be considered to determine the direction of plastic strain. Fortunately, most empirical models are related to deviator stress and the plasticity of soil is only considered in the loading direction.

With the aid of Eq. (9), the time domain dynamic stresses are obtained, and subsequently, the cycles of loads should be determined. Generally, the number of load cycles N_P can be approximated by the number of axle loads. The number of load cycles after passage of N_T trains can be calculated by

$$N_{\mathrm{P}}(n) = nN_AN_Vn = 1,2,\ldots,N_{\mathrm{T}} \tag{10}$$

where N_A denotes the number of axles in one vehicle, and N_V denotes the number of vehicles of one train. For example, the CRH2 high-speed train used in China HSR has 4*8=32 cycles. Fig. 13 shows the dynamic deviator stresses of the soil surface and the soil under 10 m. Focusing on the stresses of the soil surface, the peak magnitudes generated by the adjacent wheelsets in one bogie are close. However, the two peaks can not be respectively recorded as two load cycles with magnitudes $\mathrm{P}(t_1)$ and $\mathrm{P}(t_2)$ because the magnitude of stresses after P1 does not attenuate to zero. To deal with this problem, a practical methodology is dividing them into two load cycles with magnitude $\mathrm{P1}^*=\min\{\mathrm{P}(t_1),\mathrm{P}(t_2)\}$ and $\mathrm{P2}^*=\max\{\mathrm{P}(t_1),\mathrm{P}(t_2)\}-[\mathrm{P}(\tau)]_{\min}$ with $t_1\le\tau\le t_2$. That is, the stresses generated by one bogie can be recorded as two load cycles as shown in Fig. 14. In terms of the stresses observed at 10 m depth, we can see that the magnitudes of stresses attenuate and form one peak for a bogie. This method can also be applied to determine the smaller load cycles within $\mathrm{P1}^*$ and $\mathrm{P2}^*$. Nevertheless, the stresses of soil are a low-frequency signal, and the effects of these loads can be neglected. Similarly, by using the same criterion, one can obtain two load cycles with the larger magnitude $\mathrm{P1}^*$ and the smaller one $\mathrm{P2}^*$. Although the smaller magnitude $\mathrm{P2}^*$ has a slight effect on the predicted settlement, we still record it to meet the number of load cycles for one vehicle is equal to N_V.

A more precise statistical method for determining the number of load cycles and their magnitudes is the rain-flow counting technique [52]. This approach categorizes the load into two primary types: (1) high-cycle, low-amplitude, and (2) low-cycle, high--amplitude. In our prior research, this method was employed to quantify the load imposed by railway vehicles on railway fasteners. However, for railway subgrade soils, plastic strain is predominantly induced by low-frequency vibrations. Consequently, Eq. (10) is adequate for simulation purposes, as the number of principal stress rotations corresponds to the number of train axles.

Following the procedure detailed above, the plastic strain of the soil $\widetilde{\varepsilon}(x,y,z)$ can be calculated. It should be noted that the strain has spatial distribution and settlement of railway tracks or subgrade surface can be calculated by using the layerwise summation method:

$$\mathbf{S}(x,y) = \int \widetilde{\varepsilon}(x,y,z)\mathrm{d}z \tag{10a}$$

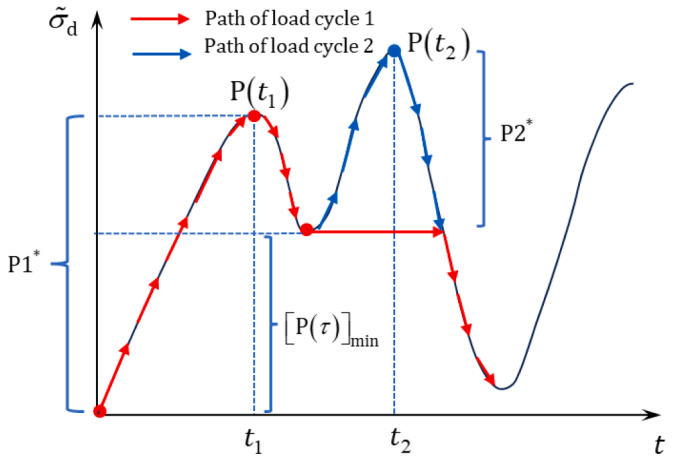

Fig. 14. The method for recording the magnitudes of load cycles generated by one bogie.

where $\mathbf{S}(x,y)$ denotes the distribution of the settlement in the x-y plane.

3.4. Verification of the Settlement Prediction Model

The present results are verified by comparing them with the results in [43,53]. Eq. (8) was used to calculate the train-induced plastic strain of soil in which the deviator stresses are obtained by empirical formula $\widetilde{\sigma}_{\mathrm{d}} = \widetilde{\sigma}_{\mathrm{d},0}\mathrm{e}^{-0.279h}$ with $\widetilde{\sigma}_{\mathrm{d},0}$ the stresses of soil surface and h the depth. The track irregularities are not considered in this case. The parameters of the model in [43] have been fully presented. Fig. 15 shows the plastic deformation observed on the soil surface. It can be seen that the plastic deformation simulated with the present models agrees well with the results in the above reference, which illustrates the validity of the settlement model.

4. Iterative framework for predicting CSTZ

Based on the two models established in Sections 2 and 3, an iterative framework is proposed in this section to predict the CSTZ. By combining the TTTZ model presented in Section 2 with the cumulative settlement prediction model proposed in Section 3, the long-term cumulative settlement of the transition zone under cyclic loads can be predicted.

Noting Eqs. (8) and (10), if the dynamic stress of soil is consistent for each train passing through the transition zone, the CSTZ can be directly calculated by:

$$\widetilde{\varepsilon}(x,y,z) = \mathbf{A}\left(\frac{\widetilde{\sigma}_{\mathrm{d}}(x,y,z)}{\widetilde{\sigma}_{\mathrm{s}}(x,y,z)}\right)^{\mathbf{M}}(N_{\mathrm{P}})^{\mathbf{B}} \tag{11a}$$

$$\mathbf{S}(x,y) = \int \widetilde{\varepsilon}(x,y,z)\mathrm{d}z = \sum_{j}\widetilde{\varepsilon}(x,y,z_j)h_j \tag{11b}$$

where $\widetilde{\varepsilon}(\mathbf{x},\mathbf{y},\mathbf{z})$, $\widetilde{\sigma}_{\mathrm{d}}(\mathbf{x},\mathbf{y},\mathbf{z})$,$\widetilde{\sigma}_{\mathrm{s}}(\mathbf{x},\mathbf{y},\mathbf{z})$ are discrete form of $\widetilde{\varepsilon}$, $\widetilde{\sigma}_{\mathrm{d}}$, $\widetilde{\sigma}_{\mathrm{s}}$, and $\mathbf{x} = [x_1 \quad x_2 \quad \dots]$, $\mathbf{y} = [y_1 \quad y_2 \quad \dots]$,$\mathbf{z} = [z_1 \quad z_2 \quad \dots]$. **A**, **B**, **M** are discrete forms of parameters a, b and m in Eq. (8) for different materials of the transition zone, and their relationship between $\widetilde{\varepsilon}$, $\widetilde{\sigma}_{\mathrm{d}}$, and $\widetilde{\sigma}_{\mathrm{s}}$ follows the point-to-point rule. h_j is the thickness of the j-th soil layer, which should be as small as enough to ensure the accuracy of prediction.

However, the dynamic stress matrix in Eq. (11) is not consistent in many cases when studying the evolution process. The occurrence of settlement causes the irregular of tracks which affects the stress $\widetilde{\sigma}_{\mathrm{d}}$ in the time domain. Hence, the stresses generated by trains is an evolution process, see Fig. 16.

In many engineering problems, the evolution of structural performance requires tremendous computations of responses. Similarly, in Section 3, the computation of CSTZ requires a large amount of computing resources. For example, if we computed the cumulative settlement for all passages of the trains, Eq. (11) should be expressed by

$$\widetilde{\varepsilon}(x,y,z) = \sum_{i}^{N_{\mathrm{T}}}\Delta\widetilde{\varepsilon}_i(x,y,z) = \sum_{i}^{N_{\mathrm{T}}}\mathbf{A}\left(\frac{\widetilde{\sigma}_{\mathrm{d},i}(x,y,z)}{\widetilde{\sigma}_{\mathrm{s}}(x,y,z)}\right)^{\mathbf{M}}\left([N_{\mathrm{P}}(i)]^{\mathbf{B}} - [N_{\mathrm{P}}(i-1)]^{\mathbf{B}}\right) \tag{12a}$$

$$\mathbf{S}_i(x,y) = \mathbf{S}_{i-1}(x,y) + \Delta\mathbf{S}_i(x,y) = \mathbf{S}_{i-1}(x,y) + \sum_{j}\Delta\widetilde{\varepsilon}_i(x,y,z_j)h_j \tag{12b}$$

where $\widetilde{\varepsilon}_i(x,y,z)$ and $\mathbf{S}_i(x,y)$ denote the cumulative plastic strain and settlement after i-th train passages, respectively. $\Delta\widetilde{\varepsilon}_i(x,y,z)$ and $\Delta\mathbf{S}_j(x,y)$ respectively denote the plastic strain increment and settlement increment when the number of train passages increase from $i-1$ to i. The accumulative number of load cycles $N_{\mathrm{P}}(i)$ can be calculated by Eq. (10). $\widetilde{\sigma}_{\mathrm{d},i}$ is the dynamic stresses generated by the i-th train, which is obtained by the TTTZ model.

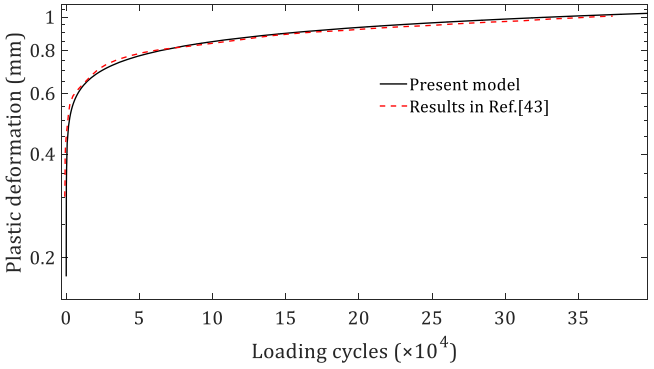

Fig. 15. Vertical plastic deformation of the subgrade.

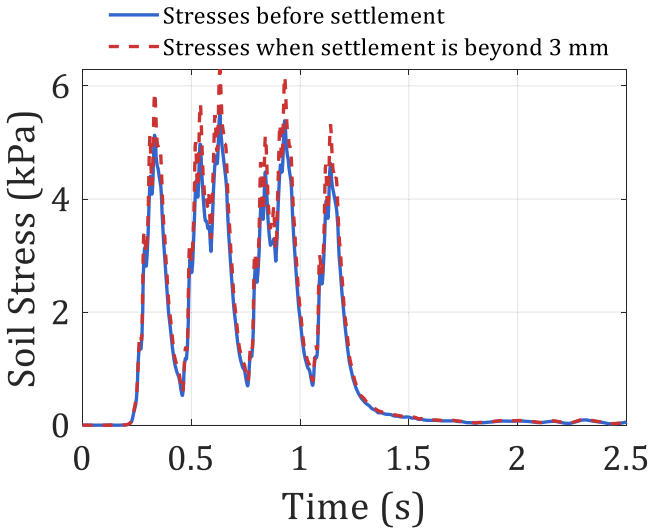

Fig. 16. Dynamic stresses of soil obtained from different periods.

To avoid successive computations of $1\sim N_{\mathrm{T}}$ trains, an iterative framework is proposed. This framework supports the linear superposition of settlement in each iteration step, avoiding the repeated computation of Eqs. (8-11) within this calculation step. This methodology is the so-called "jump step" method in Refs. [22,26,42,43].

4.1. Establishment of the iterative framework

Firstly, a proper threshold "ΔS" for the settlement increment in each iteration of the framework should be determined. Obviously, when the increment of settlement in one iteration step k is larger than ΔS, the simulation could go to the iteration step $k+1$. Based on this definition, a framework can be established as follows:

Step 1 Initializing the parameters of the framework: (i) the initial track irregularity; (ii) the threshold ΔS; (iii) the maximum number ΔN of passages of trains in each iteration; (iv) the simulation number N_{T} of passages of trains.
Step 2 Implementing the simulation of the TTTZ model and obtaining the dynamic stresses $\widetilde{\sigma}_{\mathrm{d},k}$ of the transition zone in the current iteration step k.
Step 3 Calculating the settlement increment by using Eq. (12) considering ΔN load cycles:

$$\widetilde{\varepsilon}_k(x,y,z)=\widetilde{\varepsilon}_{k-1}(x,y,z)+\Delta\widetilde{\varepsilon}_k(x,y,z)=\mathbf{A}\left(\frac{\widetilde{\sigma}_{\mathrm{d},k}(x,y,z)}{\widetilde{\sigma}_{\mathrm{s}}(x,y,z)}\right)^{\mathbf{M}}\left([N_{\mathrm{P}}(k)]^{\mathbf{B}}-[N_{\mathrm{P}}(k-1)]^{\mathbf{B}}\right) \tag{13a}$$

$$N_{\mathrm{P}}(k)=N_{\mathrm{P}}(k-1)+\Delta N N_A N_V, N_{\mathrm{P}}(0)=0, k=1,2,\ldots \tag{13b}$$

$$\mathbf{S}_k(x,y)=\mathbf{S}_{k-1}(x,y)+\Delta\mathbf{S}_k(x,y)=\mathbf{S}_{k-1}(x,y)+\sum_j\Delta\widetilde{\varepsilon}_k(x,y,z)h_j \tag{13c}$$

It should be noted that the cumulative settlement in the iteration step $k$represents a linear superposition of the results induced by ΔN passages of trains using the same stresses $\widetilde{\sigma}_{\mathrm{d},k}$ obtained from **Step 2**.

Step 4 Determine whether the settlement increment $\Delta\mathbf{S}_k(x,y)$ exceeds the threshold ΔS. If yes, reducing the number of passages of trains until $[\Delta\mathbf{S}_k(x,y)]_{\max}<\Delta S$, and the cumulative plastic strain $\widetilde{\varepsilon}_k(x,y,z)$ and settlement $\mathbf{S}_k(x,y)$ after the iteration step k is updated by replacing ΔN with the reduced number ΔN_k in Eq. (13).
Step 5 Updating the parameters of the TTTZ model. The additional rail deformation caused by the cumulative settlement $\mathbf{S}_k(x,y)$ is calculated by using the Newton-Raphson method. The additional rail deformation is regarded as the excitation of the wheel-rail contact system in the TTTZ system. Moreover, the contact relationship between the track and the soil surface also needs to be updated.
Step 6. Updating the parameters of the iterative framework: $N_{\mathrm{P}}(k)=N_{\mathrm{P}}(k-1)+\Delta N_k N_A N_V, k=k+1$.
Step 7 Repeating **Steps 2** to **6** until $N_{\mathrm{P}}(k)>N_{\mathrm{T}}$, the procedure goes to end.

To further explain the key step of the iterative framework, a schematic diagram is drawn to show the first five iteration steps. It can be seen in each iteration step, only one computation of the TTTZ model is implemented, and the settlement increment curve is directly predicted by **Steps 4** and **5**. Using this "jump method", the implementation times of computation of the TTTZ model can be reduced from ΔN to 1 for one iteration step. This methodology is widely utilized in the prediction of structural fatigue life [54]. We used this methodology as the key algorithm to achieve the prediction of train-induced settlement analysis, as shown in Fig. 17. Hereafter, the term "jump step" actually refers to the "iteration step" in this section.

Fig. 18 shows the schematic of the iterative framework architecture, illustrating its integration with the TTTZ model and the settlement prediction model. The computation of the TTTZ model is implemented only when the condition in Step 3 "$[\Delta \mathbf{S}_k(\mathbf{x},\mathbf{y})]_{\max} < \Delta S$" is met.

4.2. Convergence of the iterative framework

It is evident that the quantity of the threshold ΔS is crucial for the convergence of the framework. In Ref. [43], was empirically estimated as a small value (ΔS<0.2 mm). However, the stresses in their work are only computed using empirical formulations. The application of "ΔS=0.02 mm" in simulation continuum solid soil is unknown. To choose the best estimation of the threshold ΔS, a numerical test is necessary. Four examples are examined, namely ΔS=0.4 mm, 0.2 mm, 0.1 mm, and 0.05 mm, to study the convergence of the framework. As shown in Fig. 19, four settlement curves are predicted by the framework. It can be seen the case "ΔS=0.4 mm" shows an overestimation of the settlement development compared to the other three cases. Reducing the quantity of ΔS, the predicted settlement curve is smaller and approaches a convergence curve. After examination, "ΔS=0.2 mm" for each iteration is sufficient for simulation and is adopted in the subsequent analysis.

5. Numerical studies

In this section, a numerical investigation of the long-term train-induced settlement is presented using the iterative framework explained in Section 4. 30 iterative steps are selected to elucidate the settlement evolution characteristics and their impact on the dynamic responses of the TTTZ system. Furthermore, a time-frequency analysis method is developed to identify the dominant wavelength of the settlement along the track direction.

5.1. Simulation settings

In the TTTZ model, the train track and transition zone sub-models adopted the same parameters in Appendix A.

To ensure computational efficiency, we've opted to conduct simulations using a three-carriage model to predict the long-term settlement evolution. Our analysis reveals that, after 4×10^6 loading cycles (equivalent to 417 days of operation), the difference in settlement at a specific point (x=31.7m corresponding to the joint of the transition and subgrade zone) between the 3-carriage model and the 8-carriage model is less than 1%, indicating a high degree of agreement, as shown in Fig. 20.

Therefore, the numerical train model in numerical analysis comprises a 3-carriage model (1 motor car + 2 trailers) is employed, with detailed parameters based on CRH2, as detailed in Appendices A1 and A2. In the settlement prediction model, the values of a, b, and m in Eq. (8) are shown in Table A.5, which are adopted from [26,43]. Track irregularities with 1~100m wavelength are generated by the Chinese ballastless track average spectrum and are regarded as the initial irregularities in the first jump step, as shown in Fig. 21. The threshold "ΔS=0.2 mm" is adopted in this section, and the maximum number ΔN for trains for an iteration step is 15625 (equal to 5e6 cyclic loads).

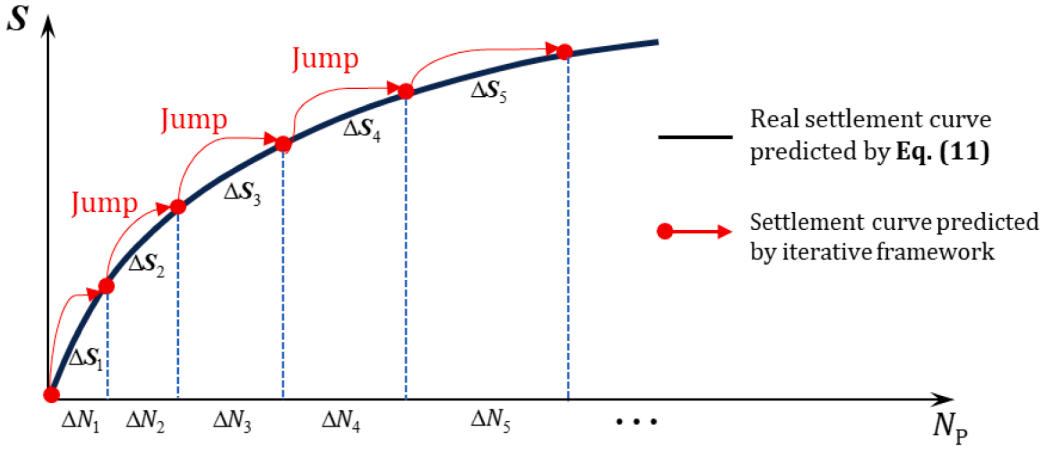

Fig. 17. Schematic diagram of the "Jump method" in the iterative framework.

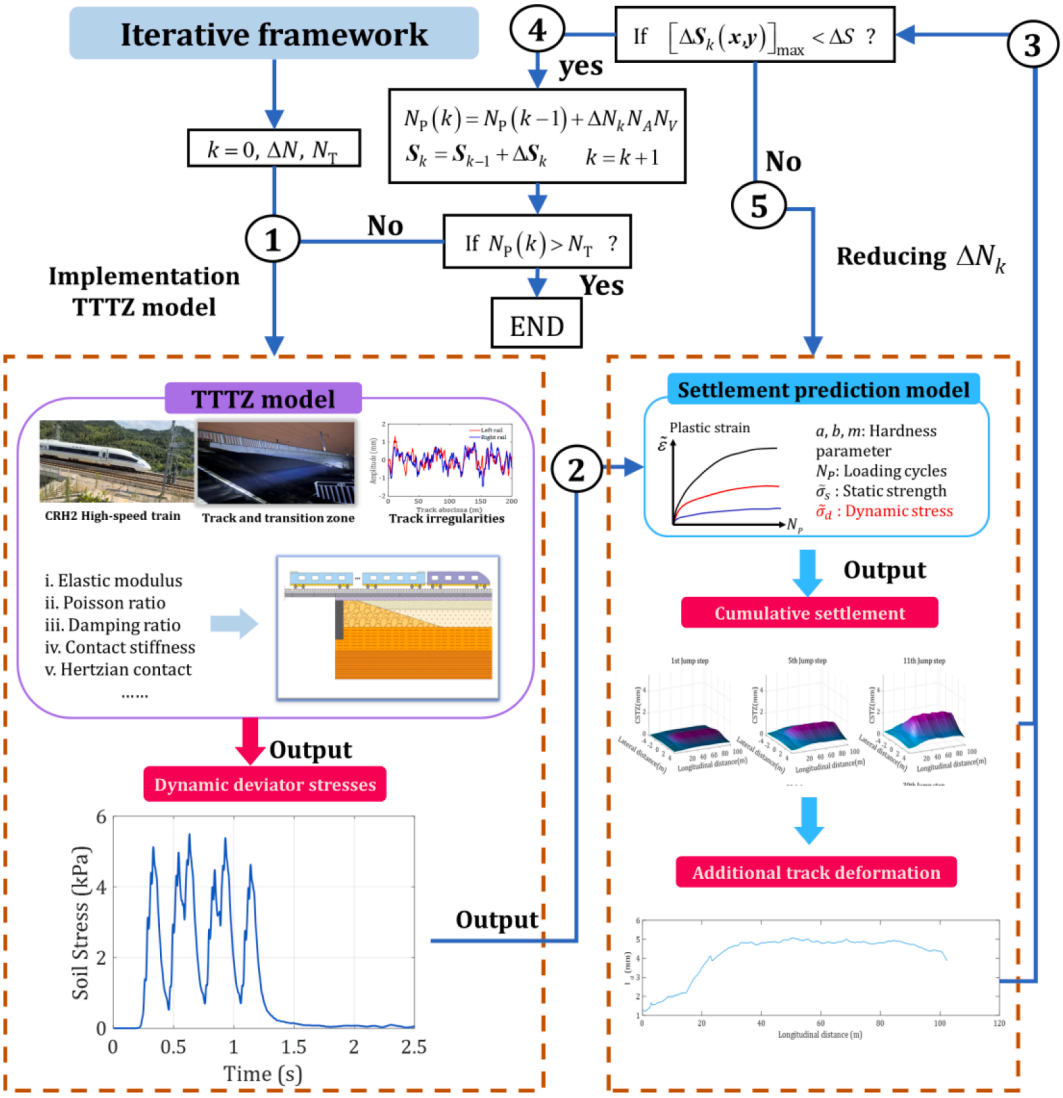

Fig. 18. The analysis framework of the iterative framework.

5.2. *Temporal-spatial evolution of the CSTZ*

5.2.1. *Evolution of the settlement in each jump step*

30 jump steps are calculated using the proposed iterative framework, and they contain 6408441 train load cycles, as listed in Table 2. The number N of jump steps (iteration step) and the corresponding number N_P of cumulative cyclic loads are listed in Table 2.

Fig. 22 shows the spatial distribution of the CSTZ after the 1st, 5th, 11th, 16th, 22nd, and 30th jump steps. The shape of the "bending angle" of the settlement can be observed on the soil surface, which agrees with the results in [26]. At the 30th jump step, the bending angle θ_S is 0.267 ‰ (refer to Fig. 1 for specific definitions), which is more than a quarter of the limit angle of 1 ‰. It can also be seen that the bending angle is highly distorted and tends to stabilize in later stages, as can be seen in Fig. 22. The relationship between the CSTZ and additional track irregularity is fully considered and calculated by using the *Newton-Raphson* method. It can be concluded from Figs. 16 and 23 that the evolution of the bending angle is consistent with that of the CSTZ.

To observe the settlement contribution of each soil layer, we calculated the settlement in the different soil layers, as shown in Fig. 24. The settlements (or the settlement rates) of the three layers of the subgrade are respectively symbolically labeled "S1", "S2" and "S3", while that of the subsoil is labeled "S4" as defined in Fig. 2. Two observation points, namely point A and point B are selected, as shown in Fig. 2. The transition subgrade is from x=3 to 23m in longitudinal direction. Fig. 24 presents the evolution of CSTZ observed at these two points. The first point A is located below the center of the track and at x=14.2 m longitudinally (transition subgrade zone) and point B is at the joint of the transition and subgrade zone, which is located below the center of the track and at x=31.7 m longitudinally (normal subgrade zone). The settlements observed at the two points show a fast increase with respect to

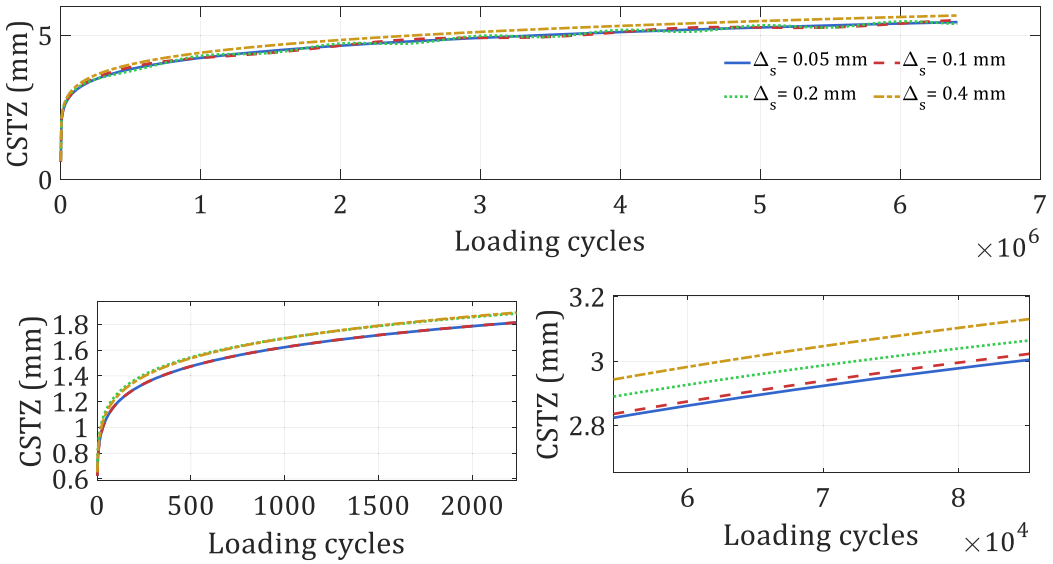

Fig. 19. CSTZ predicted by the framework using different thresholds 0.4 mm, 0.2 mm, 0.1 mm, and 0.05 mm (a. entire view of the results; b. partially enlarged view for 0~2200 cycles; c. partially enlarged view for 5.6e4~8.3e4 cycles).

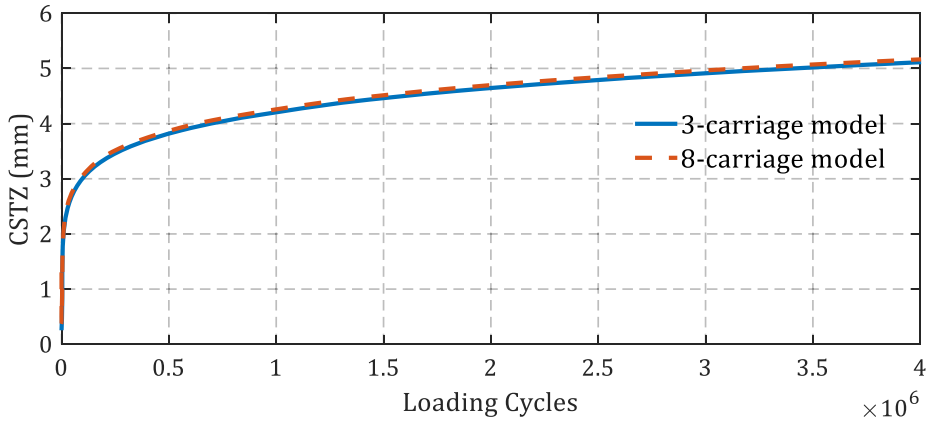

Fig. 20. The plastic deformation under the 3-carriage model and the 8-carriage model.

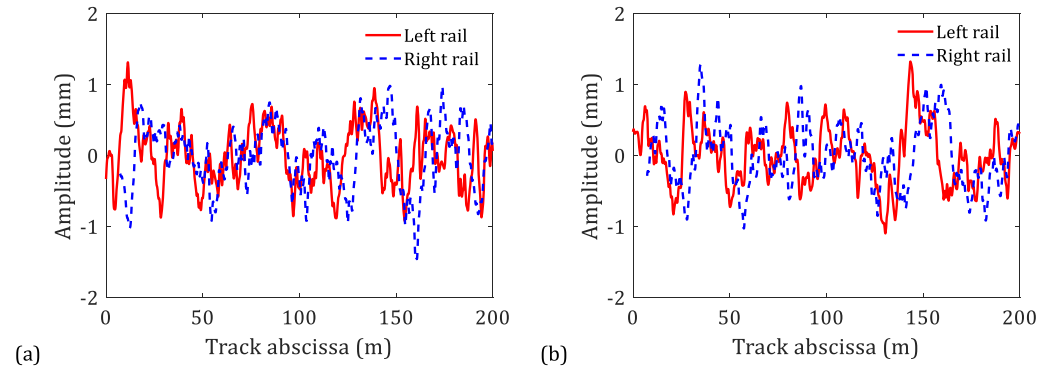

Fig. 21. Random track irregularities: mid-long wavelength component generated by China HSR spectrum (a. initial track vertical irregularities.; b. initial rail lateral irregularities).

Table 2
Number of cumulative loading cycles after each time-varying process.

N	N_P	N	N_P	N	N_P	N	N_P	N	N_P
1	1	7	2405	13	91104	19	1009445	25	3908441
2	8	8	5079	14	144423	20	1408441	26	4408441
3	38	9	9998	15	222698	21	1908441	27	4908441
4	137	10	18568	16	335074	22	2408441	28	5408441
5	406	11	32836	17	493236	23	2908441	29	5908442
6	1044	12	55690	18	711911	24	3408441	30	6408441

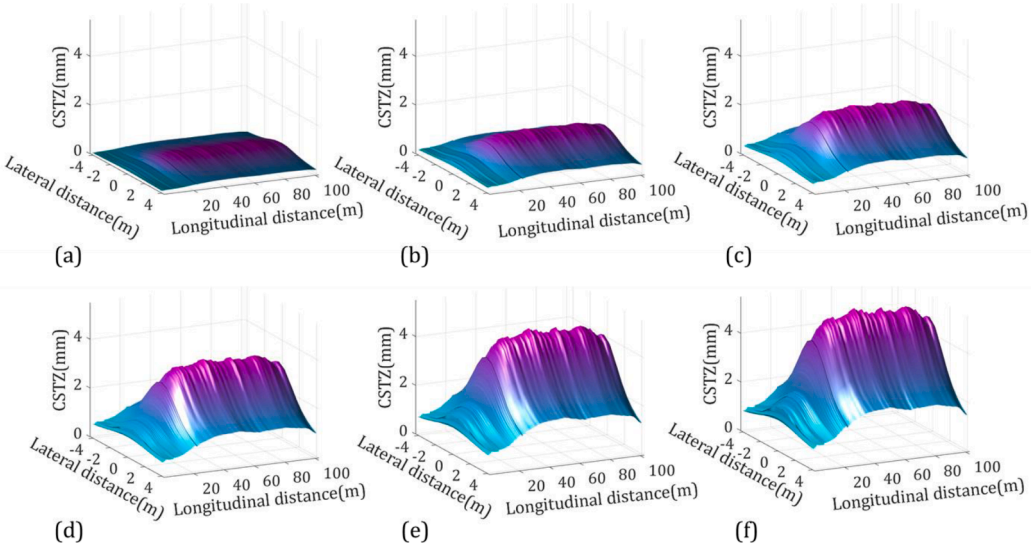

Fig. 22. CSTZ after the jump steps (a 1st; b 5th; c 11th; d 16th; e 22nd and f 30th).

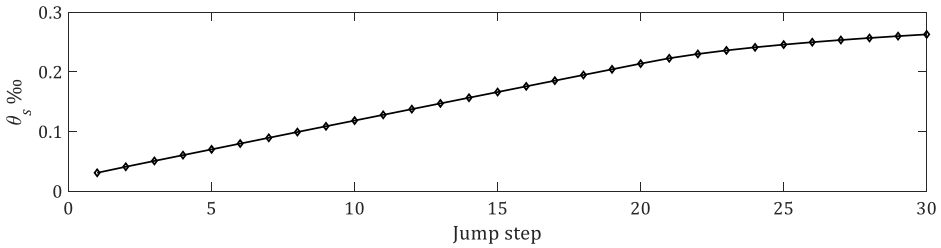

Fig. 23. Evolution of the bending angle.

loading cycles at the beginning and then the increase becomes slow, which is consistent with the results of bending angle in Fig. 23. The difference between the two observed positions is significant due to the different soil properties. The total settlement are 5.4682 mm for point A and 1.8832 mm for point B when it comes to the 30th jump step, where the settlement observed at the first point is 2 to 3.5 times larger than that of the second position. The settlement of the S1 layer is less than 0.1 mm due to its small thickness and can be neglected compared to other layers.

The contribution of each layer's cumulative settlement to the overall cumulative settlement at point A and B is quantified, as shown in Fig. 25. It can be observed that the S4 has a large proportion (53.27% to 83.29%) of the total cumulative settlement. The weight value of S4 increases at first and then decreases until it is finally constant. Moreover, the weight value of S3 contributes from 4.75% to 39.09%, from the gravel zone to the normal subgrade zone, longitudinally. In contrast, the weight value of S2 is from 23.18% to 2.83%, and the weight value of S1 is nearly 0.5% for the CSTZ. It is concluded that the main reason for the bending angle is the weight value of S3, which increases in the longitudinal direction due to the soil properties in the subgrade body under the subgrade bed.

Four representative lines (each line corresponds to a specific location in the longitudinal direction as shown in Fig. 2) are selected to study the stress and cumulative plastic strain ϖ along the depth of the soil, as shown in Fig. 26 (blue lines). Line 1 is located at 5.5 m longitudinally in the graded gravel zone. Line 2 and 3 are located below the track centre and at 13 m and 18 m longitudinally respectively, in the transition zone of the subgrade, and line 4 is located at 28 m in the normal subgrade zone. When the 1st wheelset

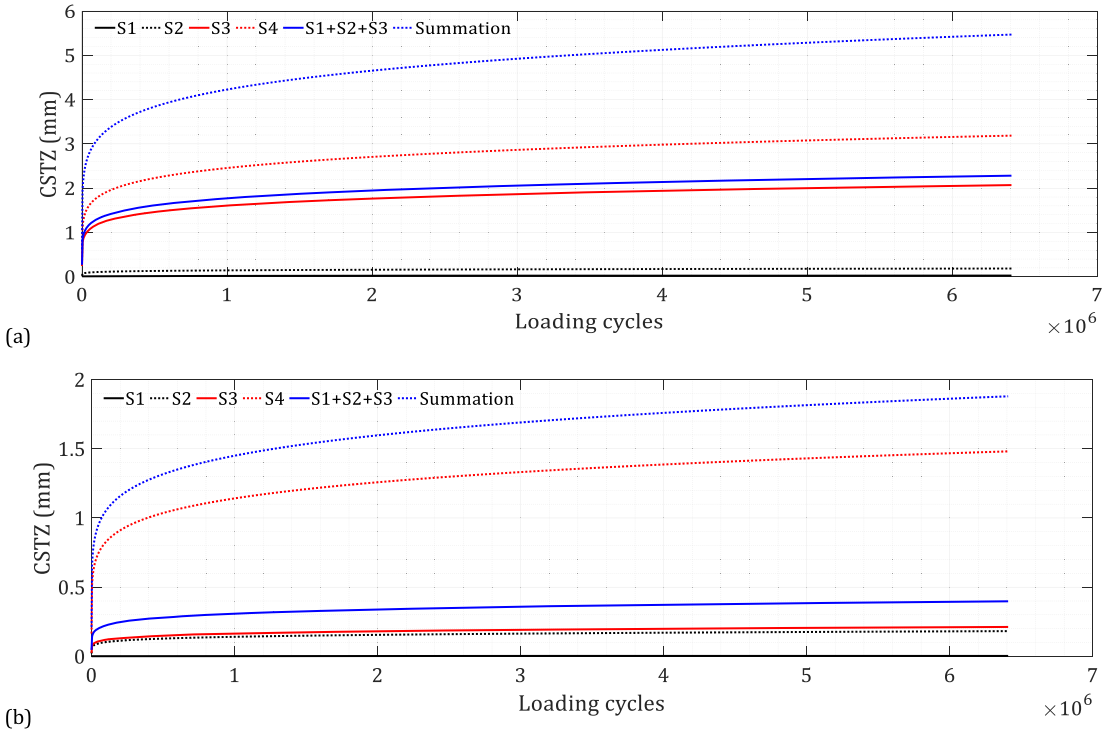

Fig. 24. Evolution and varying gradient of the CSTZ at two specific points (a. evolution of the CSTZ at the first point; b. evolution of the CDS at the second point).

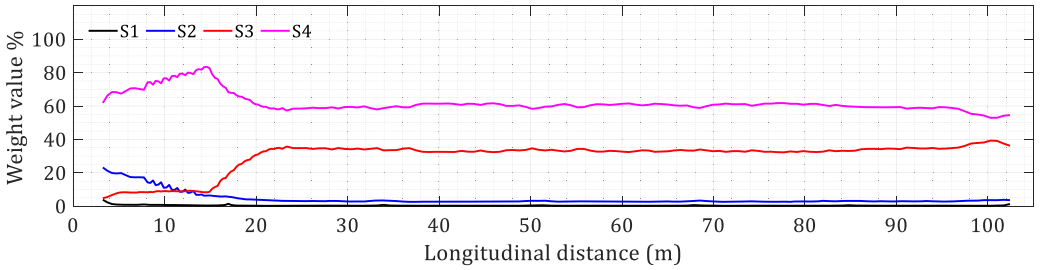

Fig. 25. Weight values of each layer's cumulative deformation to the CSTZ at the 30th jump step.

reaches the four lines, the corresponding time moments are 0.297s, 0.387s, 0.447s, and 0.576s. The stresses and ϖ induced by the 1st wheelset are calculated, as shown in Fig. 26. The stress changes abruptly at the interface between the subgrade and the subsoil, which is due to the large differences in material properties. The trend of the subsoil is the same as that of the subgrade. The trend of ϖ is similar to the stress; however, the only difference is that ϖ decreases slowly at the interface without abrupt change. Fig. 26(b) and Fig. 26(c) show the stress distribution and ϖ along the second and the third lines, which are both located in the transition subgrade zone. Due to the different properties of the layered soil, it can be clearly seen that the position of the changing abrupt stress and ϖ are the interface of the different soil layers along the depth. The maximum stress and ϖ occurs at the interface between the subgrade and the gravel layer, as the soil properties between these layers are very different. The ϖ of the subgrade body under the subgrade bed layer is much larger than that of the other soil layers due to the soft soil properties, as shown in Fig. 26(c) and Fig. 26(d).

The track irregularities caused by the train-induced settlement are combined with the initial track irregularities, which influence the wheel-rail forces. Due to the variation of the origin track irregularities, the different settlement worsens or improves the dynamic performance of the wheel-rail interaction, as shown in Fig. 27. The stress evolution rules (shown in Fig. 26) observed at different lines follow the same change trend with the wheel-rail forces. Either an increase or decrease in wheel-rail forces depends on whether the additional track irregularities mitigate or exacerbate the initial irregularities.

5.2.2. Identification of the area with severe settlement

The severe settlement area should be identified due to its significant impact on train-track interaction. Meanwhile, identifying those areas makes it convenient for railway settlement-related maintenance. However, traditional time-frequency methods cannot process

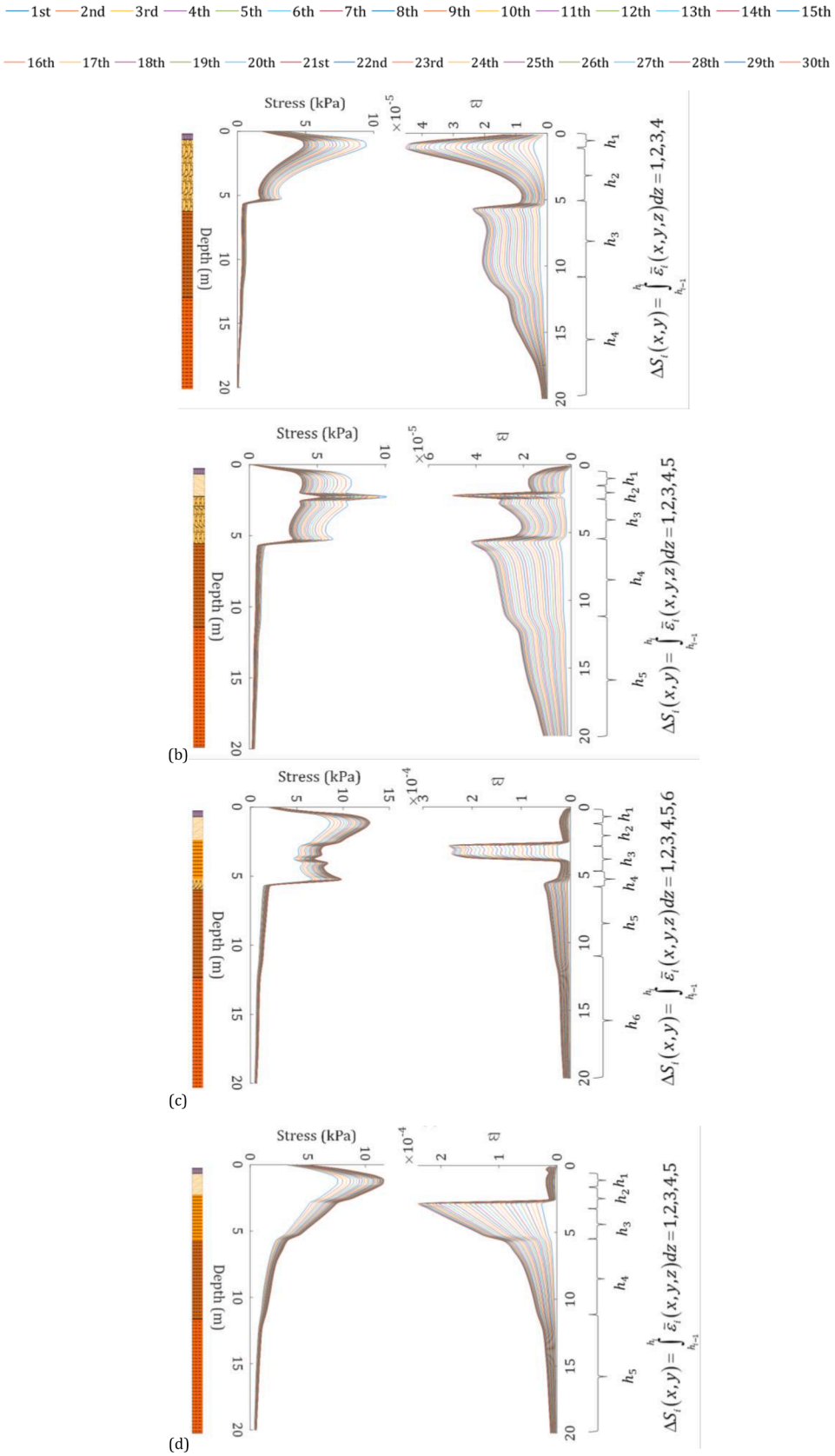

(caption on next page)

Fig. 26. The temporal evolution of the stress and the cumulative plastic strain distribution (**a.** Line 1; **b.** Line 2; c. Line 3; d. Line 4).

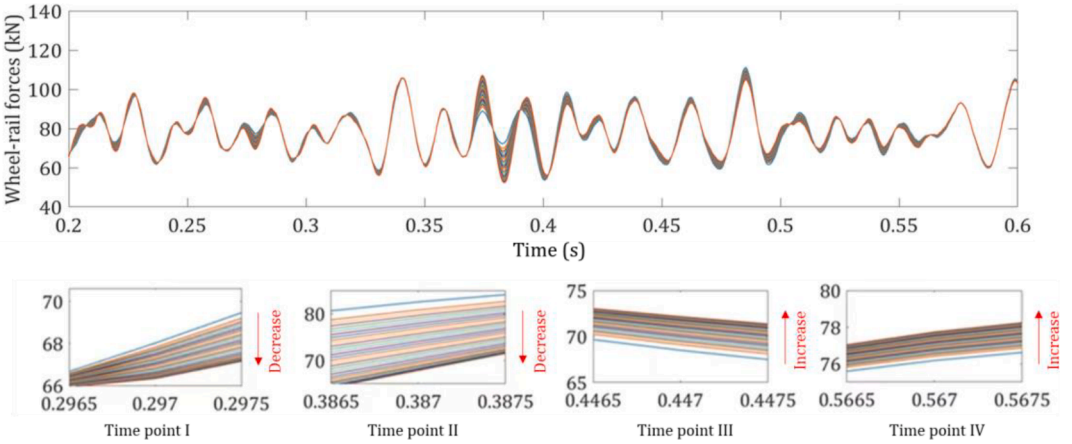

Fig. 27. The temporal evolution of the wheel-rail forces at the four points in time.

this problem very well due to the boundary effect of settlement signals and low resolution in the spatial domain. In this paper, a novel time-frequency method based on Wavelet transform and short-time energy is proposed to extract the average energy density distribution of settlement and identify the severe settlement areas according to their energy density. The proposed method has a better resolution than the traditional time-frequency approaches in the space domain. The detailed procedure is organized as:

Step 1 Dividing the spatial distribution of settlement into several signals $S_1(x)$, $S_2(x)$,…, $S_n(x)$, in which each signal is the function of longitudinal position x;

Step 2 Adopting the Continuous Wavelet transform [55,56] to obtain the continuous wavelet coefficients of $S_1(x)$, $S_2(x)$,…, $S_n(x)$:

$$W_{\psi,i}(\upsilon,\tau)=\frac{1}{\sqrt{|\upsilon|}}\int_{-\infty}^{+\infty}S_i(x)\psi*\left(\frac{x-\tau}{\upsilon}\right)\mathrm{d}x \tag{12}$$

where $W_{\psi,i}(\upsilon,\tau)$ is the continuous wavelet coefficient of the $S_i(x)$; $\psi(x)$ is the Wavelet basis function and $\psi*(x)$ is its conjugation; υ and τ are the scale and shift factors, respectively.

Step 3 Reconstructing the signal components of $S_1(x)$, $S_2(x)$,…, $S_n(x)$ at different frequency bands of $\left\{\Omega_{s,1},\Omega_{s,2},\ldots,\Omega_{s,N}\right\}\in\Omega_{s,N}$ by using the inverse Wavelet transform:

$$S_i\left(x,\Omega_{s,j}\right)=\frac{1}{C_\psi}\int_{\upsilon_{\mathrm{low},j}}^{\upsilon_{\mathrm{high},j}}\frac{\int_{-\infty}^{+\infty}W_{\psi,i}(\upsilon,\tau)\psi_{\tau,\upsilon}(x)\mathrm{d}\tau}{\upsilon^2}\mathrm{d}\upsilon \tag{13}$$

with $\psi_{\tau,\upsilon}(x)=\frac{1}{\sqrt{|\upsilon|}}\psi\left(\frac{x-\tau}{\upsilon}\right)$ being the Wavelet basis function after scale processing $x=x/\upsilon$ and shift processing $x=x-\tau$; $\Omega_{s,j}$ are the spatial frequency of signals $S_j(x)$. where $\overline{S}_i\left(x,\Omega_{s,j}\right)$ is the settlement signal after being filtered; $\Omega_{s,j}\in\Omega_s$ are the sub-frequency bands; $\upsilon_{\mathrm{high},j}$ and $\upsilon_{\mathrm{low},j}$ are the range of integration with respect to the scale factor υ, which can be calculated by

$$\upsilon_{\mathrm{high},j}=\frac{f_c}{\min\left(\Omega_{s,j}\right)},\upsilon_{low,j}=\frac{f_c}{\max\left(\Omega_{s,j}\right)} \tag{14}$$

where f_c is the centre frequency of $\psi(x)$.

C_ψ is the reconstruction constant of the Wavelet function $\psi(x)$, which needs to satisfy the admissibility condition:

$$C_\psi=\int_{-\infty}^{+\infty}\frac{|\widehat{\psi}(f)|^2}{|f|}\mathrm{d}f<\infty \tag{15}$$

in which $\widehat{\psi}(f)$ is the Fourier transform of $\psi(x)$;

Step 4 Assembling$S_1(x)$, $S_2(x)$,…, $S_n(x)$ as a matrix

$$\mathbf{S}(x,\Omega_{s,j}) = [S_1(x) \quad S_1(x) \quad \ldots \quad S_1(x)] \tag{16}$$

Step 5 Utilizing the short-time energy method to gather the signal energy along the x direction

$$\mathbf{E}(x,\Omega_{s,j}) = \begin{cases} \left|\frac{\int_0^{x+L}\mathbf{S}^2(x,\Omega_{s,j})h(L_w-x,2L,2L_w)\mathrm{d}x}{L_{S,1}}\right| \text{for} 0 < x < L_w \\ \left|\frac{\int_{x-L}^{x+L}\mathbf{S}^2(x,\Omega_{s,j})h(0,2L_w,2L_w)\mathrm{d}x}{L_{S,2}}\right| \text{for} L_w \le x \le x_2 - L_w \\ \left|\frac{\int_{x-L}^{x_2}\mathbf{S}^2(x,\Omega_{s,j})h(0,L_w+x_2-x,2L_w)\mathrm{d}x}{L_{S,3}}\right| \text{for} x_2 - L_w < x < x_2 \end{cases} \tag{17}$$

$$L_{S,1} = L_w + x, L_{S,2} = 2L_w, L_{S,3} = L_w + x_2 - x \tag{18}$$

with $h(c,d,L) = 0.54 - 0.46\cos\left(\frac{2\pi x}{L}\right), x \in (c,d)$ is the hamming window with a window length of L; where $\mathbf{E}(x,\Omega_{s,j})$ is the time-varying average energy of the signal matrices $\mathbf{S}(x,\Omega_{s,j})$; $0 \sim x_2$ is the longitudinal range of $\mathbf{S}(x,\Omega_{s,j})$; L_w is the half length of the window function; $L_{S,1}$, $L_{S,2}$, and $L_{S,3}$ are the three window cut-off lengths for three cases, which are set to deal with the signal boundary.

Step 6 Calculating the total energy density of $\mathbf{S}(x,\Omega_{s,1})$, $\mathbf{S}(x,\Omega_{s,2})$,…,$\mathbf{S}(x,\Omega_{s,1})$

$$E^*(x) = \sum_j^N \int \mathbf{E}(x,\Omega_{s,j})\mathbf{d}\Omega_s \tag{19}$$

where $E^*(x)$ is the total average energy density of the settlement.

Two wavelength regions are set here, namely 0-2 m and 2-30 m. The lower wavelength range of 0-2 m means high-frequency components, which deteriorates the wheel-rail forces. The higher wavelength range of 2-30 m could impact the car body acceleration. It should be noted that the length of the transition zone is 20 m (as shown in Fig. 2), and the up limit of wavelength of 30 m is

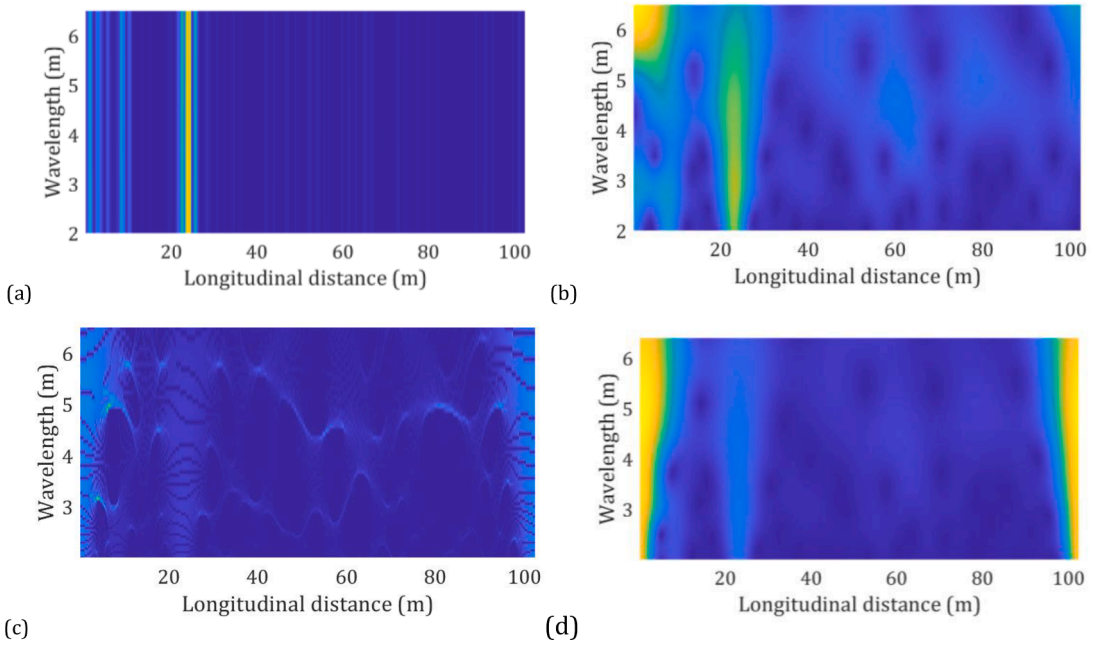

Fig. 28. Comparison of the proposed method with other traditional time-frequency methods ((a) The proposed model; (b) Wavelet transform; (c) Wavelet Synchrosuqeezed transform; (d) Generalized Stockwell transform) at energy density at 0-2 m wavelength range.

sufficient for analysis.

The settlement predicted after the 1st jump step (the first sub-plot of Fig. 22) is implemented as an illustrative example to show the advantages of the proposed time-frequency identification method. Daubechies 6 (db6) is selected as the basis function for wavelet transformation. The wavelet family "Daubechies 6"[55] is used in the present study. Following the proposed time-frequency method, the average energy density of the settlement $\mathbf{E}(x, \Omega_{s,j})$ in the space-wavelength plane is calculated, as shown in Fig. 28. To demonstrate the advantage of the proposed method, results obtained by other time-frequency approaches (Wavelet transform, Wavelet synchrosqueezed transform and Generalized Stockwell transform) are compared. As can be seen from the comparison results, the energy density calculated by the proposed model has a higher resolution ratio than the other three time-frequency approaches. In comparison with the Wavelet transform, it can be seen that although the traditional Wavelet transform has good performance in processing boundary effects for the 0-2 m case, it is not able to determine the serious settlement area for the 2-30 m case due to the strong boundary effects (Fig. 29).

The traditional time-frequency methods can identify the approximate locations of severe settlement at 0-2 m settlement wavelength region only, such as 7-11 m and 20-23 m at the transition zone (Fig. 30). However, the proposed method can determine the specific locations, such as 1.5 m, 8.5 m, 23.8 m, and 25.7 m. They are high-frequency components that may cause the degradation of wheel-rail interaction. The severe settlement areas are identified to be located at the bridge abutment zone (1.5 m), the transition zone (8.5), and the junction of the transition zone and the normal subgrade zone (23.8 m), respectively. It can be seen that the settlement at the junction of the transition zone and the normal subgrade zone has the greatest energy density, which indicates that the wheel-rail interaction could be significantly affected in this area. Furthermore, the proposed method has advantages in processing the boundary effects compared to the Wavelet synchrosqueezed transform and the generalized Stockwell transform, which demonstrates the advantage of the proposed method in dealing with the signal boundary.

As for the 2-30 m case, the proposed method can still identify two severe settlement areas, namely 1.77 m and 23.15 m (Fig. 31), which are located at the bridge abutment zone and the junction of the transition zone and the normal subgrade zone, respectively. As for the normal subgrade zone, the settlement is not uneven like the transition zone, thus the signal energy at 2-30 m wavelength is lower than that of the transition zone.

In the current analysis, the db6 wavelet from MATLAB's built-in wavelet family was selected as the basis function for wavelet decomposition. This specific wavelet configuration demonstrates superior performance in detecting anomalous signal patterns, particularly in identifying local singularities (including peak discontinuities and periodic fluctuations) and characterizing multi-scale wavelength components within the 0-2 m and 2-30 m spectral ranges [55]. The db6 wavelet's mathematical properties–specifically its six vanishing moments and compact support characteristics–provide optimal time-frequency localization for processing settlement monitoring data from transition zones. These attributes enable effective separation of high-frequency anomalous components from low-frequency trend terms through multi-resolution analysis. Notably, the elimination of baseline drift artifacts was achieved by strategically discarding approximation coefficients during signal reconstruction, while preserving critical detail coefficients corresponding to soil settlement. In this section, the selection criteria for db6 were rigorously established based on wavelet theory fundamentals and domain-specific requirements for railway transition zone monitoring.

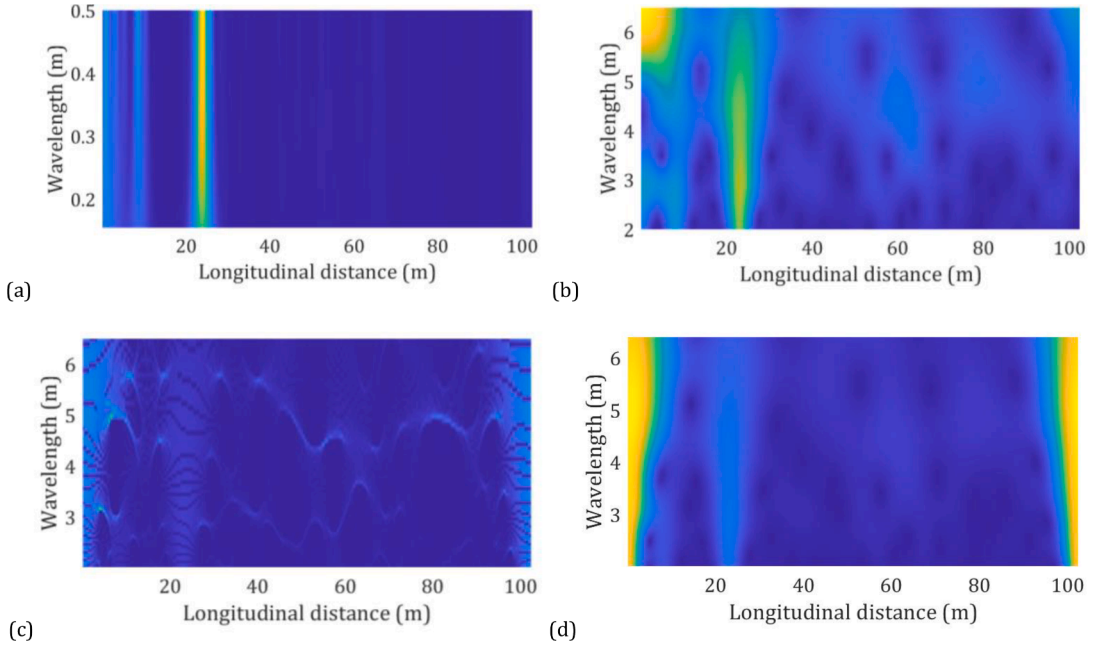

Fig. 29. Comparison of the proposed method with other traditional time-frequency methods ((a) The proposed model; (b) Wavelet transform; (c) Wavelet Synchrosuqeezed transform; (d) Generalized Stockwell transform) at energy density at 2-30 m wavelength range.

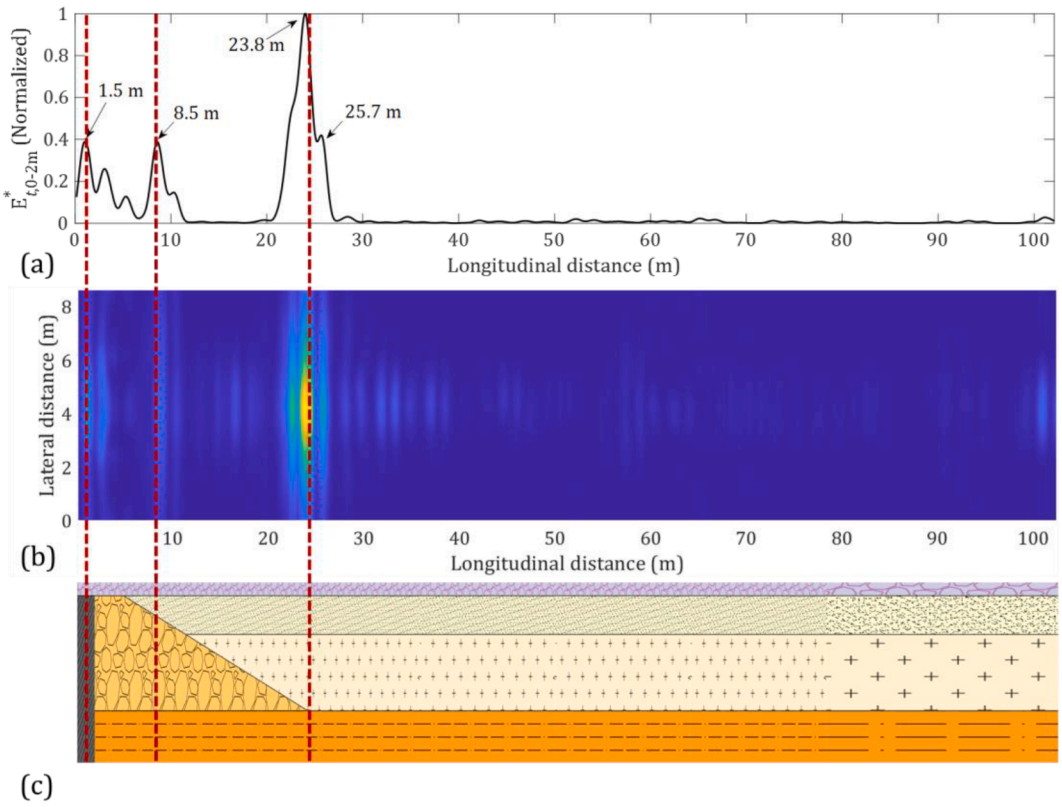

Fig. 30. (a) energy density of the settlement at 0-2 m wavelength; (b) spatial distribution of the energy density of the settlement observed in the topsoil; (c) schematic of the transition zone.

In addition, we have reconstructed the original signal from the time-space results obtained employing the widely used wavelet basis functions provided by Matlab built-in functions (Symlet wavelet "sym6, sym8", biorthogonal wavelet "bior4.4, bior5.5", orthogonal wavelet "db5, db6"). It is found that the db6 wavelet basis function adopted in the inverse wavelet transformation has the smallest error. In other words, it means that the space-frequency result obtained by db6 carries the most precise information of the original signal, compared with other basis functions. Upon justification of the choice of db6 by previous arguments, Fig. 32 compares the identified results using different Wavelet families. It can be seen that the bior5.5 and db5 are less accurate compared to other functions that provide similar results to those of db6. Therefore, db6 is the most suitable for the settlement signal analysis in this paper.

5.3. Evolution of the TTTZ system

In this subsection, the evolution of CSTZ and responses of the train-track system are discussed.

5.3.1. Evolution of systems excitation

The track vertical degradation induced by the CSTZ is an additional irregularity that influences the wheel-rail contact. 6 representative track vertical irregularities were selected for analysis, namely the settlement-induced rail deformation after the 1st, 5th, 11th, 16th, 22nd, and 30th jump steps to describe the evolution of the system excitation.

Fig. 33 shows the rail deformation induced by settlement (denoted as I_a), where its analysis length in the longitudinal direction is identical to the transition zone (Fig. 2). Moreover, the neighboring baseplates' gaps generate the enlargement of rail deformation, which belongs to short wavelength components. The track quality index (TQI [57]) is introduced to evaluate the degradation degree of the rail irregularities under the settlement. The TQI of the track vertical irregularities is calculated as follows:

$$\begin{cases} \mathrm{TQI} = \sqrt{\dfrac{1}{n}\sum_{i=1}^{n}\left(I_a(i) - \bar{I}_a\right)^2} \\ \bar{I}_a = \dfrac{1}{n}\sum_{i=1}^{n} I_a(i) \end{cases} \tag{20}$$

Fig. 34 shows the TQI of the overall vertical track irregularity. It can be observed that a trend for fast change and then slowing down is consistent with the growth of CSTZ. For the left rail, the TQI values increase from 0.148 to 1.276 as the CSTZ develops. After 222698

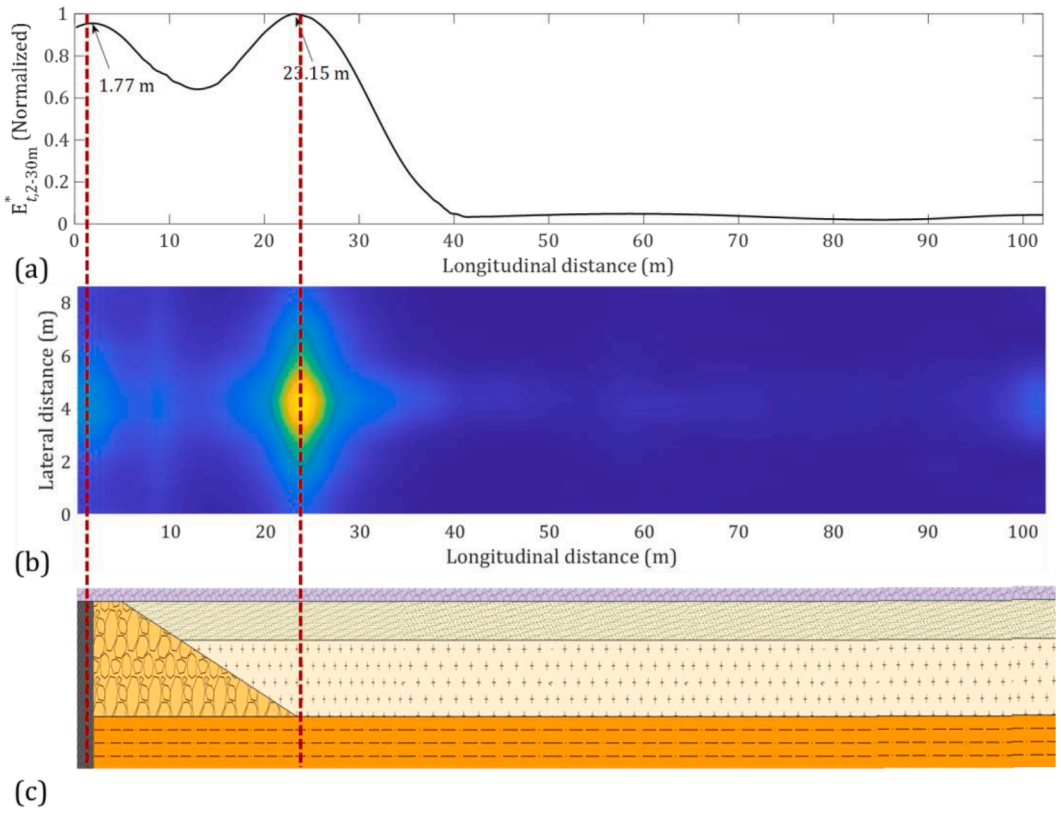

Fig. 31. (a) energy density of the settlement at 2-30 m wavelength; (b) spatial distribution of the energy density of the settlement observed in the topsoil; (c) schematic of the transition zone.

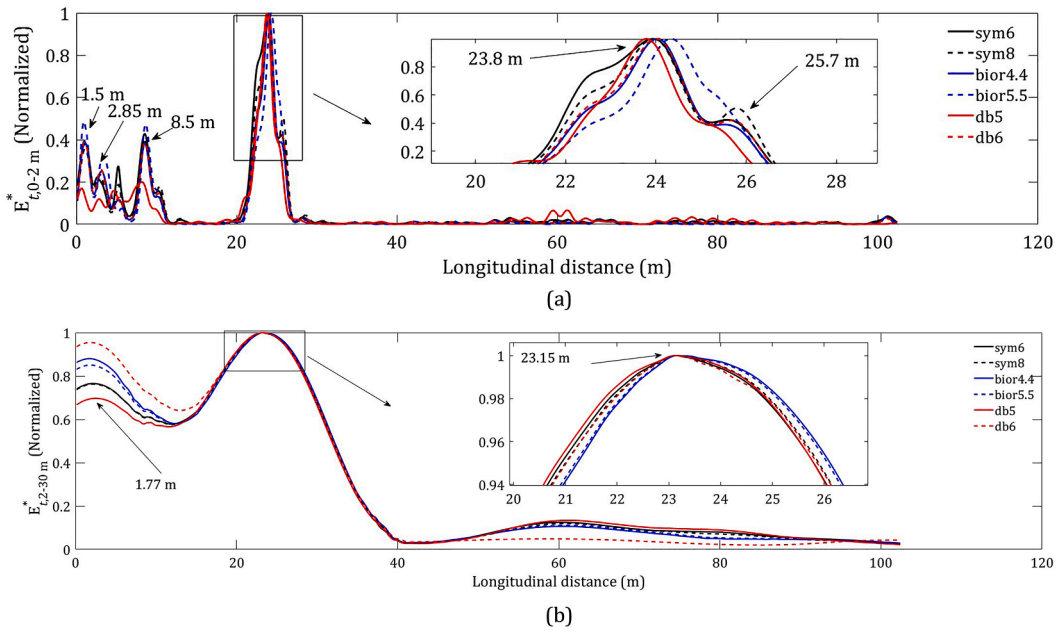

Fig. 32. Comparison of the identified results of the serious settlement locations by using different Wavelet families: (a) energy density of the settlement at 0-2 m wavelength; (b) energy density of the settlement at 2-30 m wavelength.

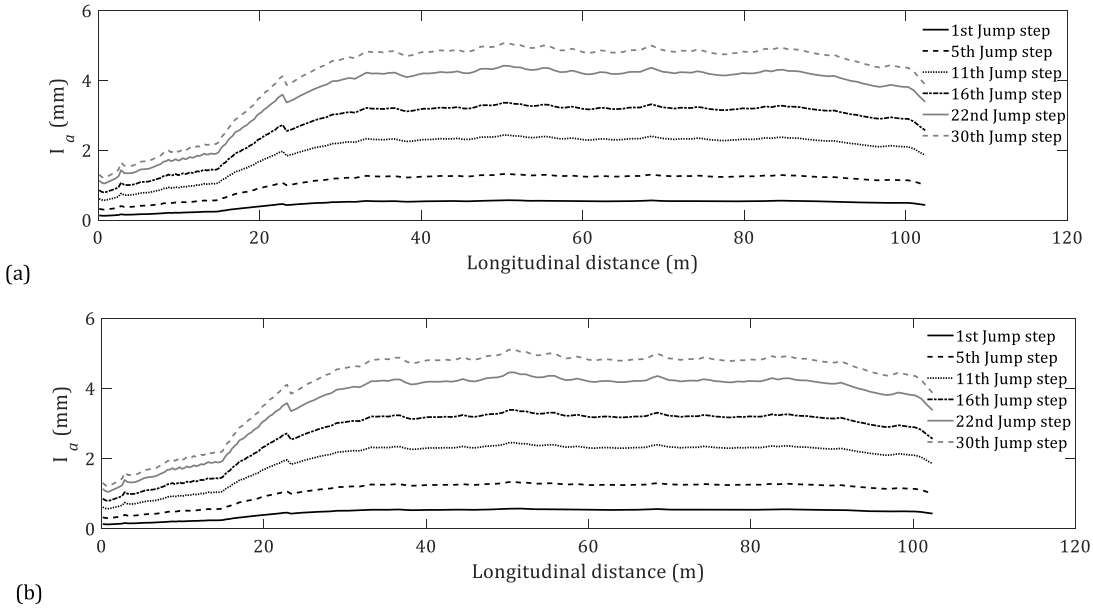

Fig. 33. Evolution of the additional deformation of the rail induced by the settlement (a. the left rail; b. the right rail).

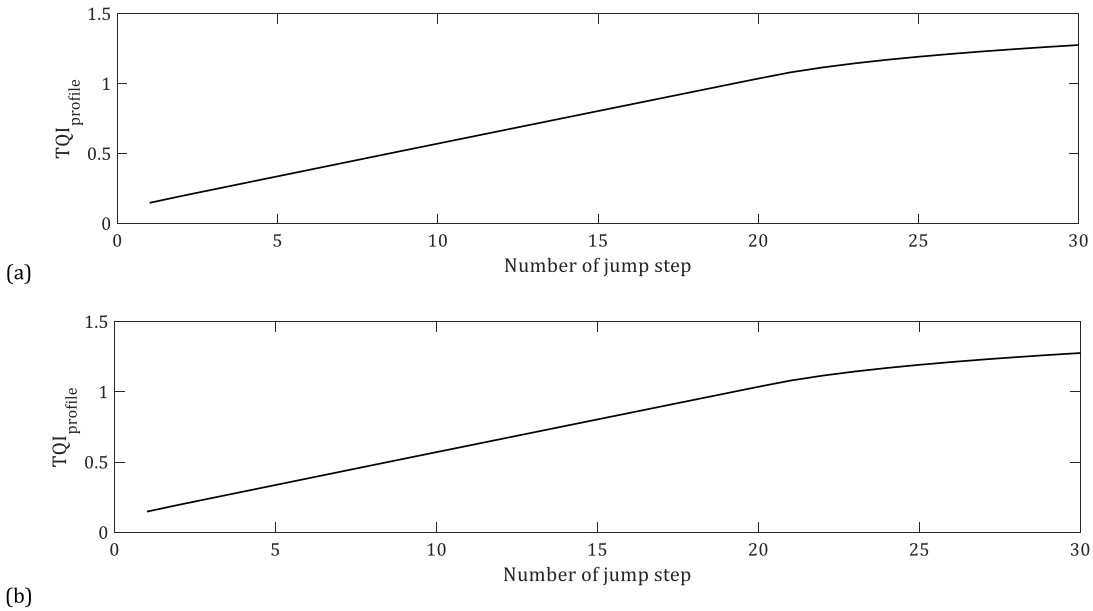

Fig. 34. Evolution of the TQI values of track vertical irregularities induced by the settlement (a. the left rail; b. the right rail).

train loads (the 15th jump step), the TQI values are 0.8043 for the left rail and 0.8041 for the right rail, which is above the TQI limit value of 0.8. This shows that the settlement in the transition zone has a significant and long-term impact on the smoothness of the track.

5.3.2. Evolution of responses of the TTTZ system

The maximum value of the vertical acceleration of the railcar body increases significantly with the temporal evolution, as shown in Fig. 35. For the motor car, with the development of settlement, the maximum value of the acceleration of the car body increases from 0.0062 g to 0.0106 g. For the 1st trailer. The maximum value of the acceleration of the car body increases from 0.0076 g to 0.0116 g during the settlement growth. Moreover, the maximum value of the acceleration of the car body for the 2nd trailer increases from 0.0047 g to 0.085 g following the growth of settlement. It can be observed that the maximum value of the vertical acceleration of the railcar body for the 2nd trailer is larger than that of other vehicles which is due to the influence of the front and rear vehicles. In contrast, the maximum value of lateral acceleration of the railcar body is low with the temporal evolution.

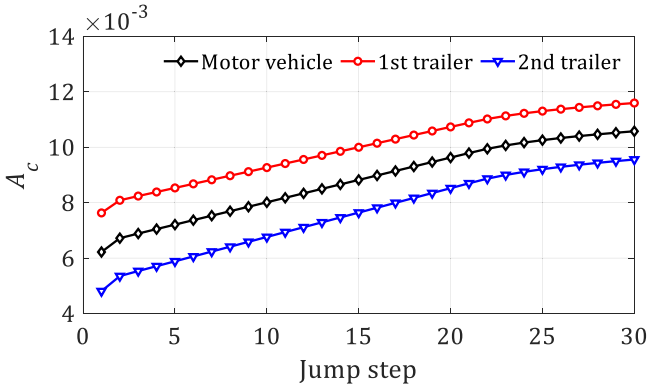

Fig. 35. Evolution curve of the maximum A_C.

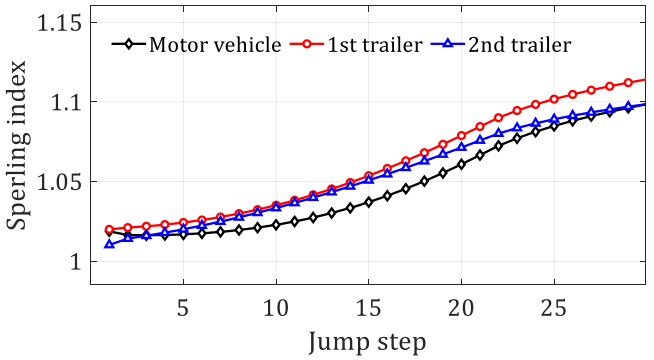

Fig. 36. Evolution curve of the Sperling index.

The running stability of the vehicle deserves to be investigated. According to the international standard, the "Sperling index" is calculated as shown in Fig. 36. For the motor car, the vertical Sperling index initially decreases and then increases sustainably. The reason for this is that the additional irregularity can first improve and then worsen the initial irregularity. For trailers, the trend of the vertical Sperling index is similar to the evolution of the maximum acceleration. The stability decreases as the Sperling index increases. Similarly, the CSZT does not influence the lateral Sperling index.

Fig. 37 shows the evolution curve of the maximum acceleration of the soil. The trend of the acceleration induced by the motor car increases from 2.23 m /s^2 to 3.31 m /s^2 with the settlement increase. For the 1st trailer and the 2nd trailer, the maximum acceleration of the soil first decreases and then increases, the range of change is from 2.31 to 3.98 m /s^2 and from 2.18 to 4.12 m /s^2 respectively.

6. Concluding remarks

In this study, an innovative iterative framework integrating a dynamic train-track-transition zone coupled model with a settlement

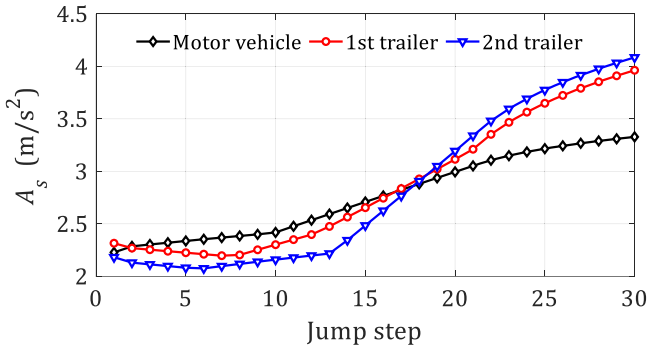

Fig. 37. Evolution curve of the dynamic response of the soil.

prediction model has been developed to investigate the long-term train-induced settlement and its spatial-temporal evolution characteristics. A jump-step method is introduced to establish the interaction mechanism between the two models and to implement the iterative algorithm efficiently. Extensive numerical simulations involving 30 jump steps and 6,408,441 cyclic train load applications are conducted to systematically analyze the time-dependent dynamic responses and their effects on settlement prediction. The principal scientific contribution of this work lies in the development of a comprehensive and robust simulation framework for predicting long-term settlement under cyclic train loading in railway transition zones. The key findings are summarized as follows:

(1) The train-induced settlement in the transition zone demonstrates distinct evolutionary characteristics that are effectively captured through the jump-step analysis. The longitudinal variation in soil mechanical properties within the transition zone results in differential track settlement and the development of rail bending angles, which significantly affect track geometry and vehicle dynamics.
(2) The cumulative settlement induced by train loading exhibits a nonlinear development pattern characterized by an initially rapid progression followed by gradual stabilization. The settlement rate can be quantitatively determined through temporal evolution analysis of the settlement curve at the point of maximum displacement, providing valuable insights for maintenance scheduling and intervention strategies.
(3) With increasing loading cycles, additional track irregularities develop due to the progressive uneven settlement in the transition zone. The spatial evolution of these irregularities differentially affects wheel-rail interaction forces, with the extent and direction of variation depending on whether the new irregularities decrease for or amplify pre-existing track defects.
(4) A novel time-frequency analysis method combining Wavelet transform and short-time energy has been developed, demonstrating superior capability in identifying critical settlement areas. The identification criterion is based on the energy density of settlement curves within the frequency band excited by wheel-rail contact forces. Comparative analyses demonstrate that the proposed approach offers superior temporal resolution and localization accuracy compared to conventional time–frequency methods.. The results indicate that the interface between the transition zone and normal subgrade is most susceptible to severe settlement accumulation.

This research provides comprehensive insights into the short-term coupled dynamic behavior and long-term settlement evolution of railway transition zones. The proposed integrated framework successfully captures the complex interaction between settlement development and dynamic system performance, bridging the gap between short-term dynamic analysis and long-term degradation prediction. The findings offer valuable theoretical and practical implications for the design, maintenance, and rehabilitation of railway transition zones.

CRediT authorship contribution statement

Borong Peng: Writing – original draft, Software, Formal analysis. **Karel N. Van Dalen:** Methodology, Investigation, Formal analysis. **Zheng Li:** Writing – review & editing, Methodology, Formal analysis, Conceptualization. **Sakdirat Kaewunruen:** Writing – review & editing, Investigation. **Lei Xu:** Validation, Funding acquisition, Formal analysis. **Jim Shiau:** Writing – review & editing, Investigation. **Tao Lu:** Writing – review & editing, Methodology, Funding acquisition, Conceptualization.

Declaration of competing interest

The authors declare that they have no known competing financial interests or personal relationships that could have appeared to influence the work reported in this paper.

Data availability

All data, models, or codes that support the findings of this study are available from the corresponding author upon reasonable request.

Acknowledgments

The first author highly appreciates Prof. Xuhui He and Dr. Yunlong Guo, for their help and dedication to improving the paper's quality. This work is supported by the National Natural Science Foundation of China (grant Nos. 52108420; 52378468; 52008404; 52278470); the Scientific Research and Development Program of China State Railway Group Co., Ltd. (N2023G083); the Science and Technology Research and Development Program Project of China National Railway Group Co., LTD (Grant Nos. L2022G007).

Supplementary materials

Supplementary material associated with this article can be found, in the online version, at doi:10.1016/j.jsv.2025.119360.

Appendix A. Model parameters

Table A.1
Parameters of the motor vehicle [40].

Parameters (Unit)	Value
The mass of the car body (kg)	48000
The mass of the bogie (kg)	3200
The mass of the wheelset (kg)	2400
The moment of inertia of the car body about X-axis (kg·m^2)	115000
The moment of inertia of the car body about Y-axis (kg·m^2)	2700000
The moment of inertia of the car body about Z-axis (kg·m^2)	2700000
The moment of inertia of the bogie about X-axis (kg·m^2)	3200
The moment of inertia of the bogie about Y-axis (kg·m^2)	7200
The moment of inertia of the bogie about Z-axis (kg·m^2)	6800
The moment of inertia of the wheelset about X-axis (kg·m^2)	1200
The moment of inertia of the wheelset about Y-axis (kg·m^2)	200
The moment of inertia of the wheelset about Z-axis (kg·m^2)	1200
The stiffness coefficient of the primary suspension along X-axis (MN/m)	9
The stiffness coefficient of the primary suspension along Y-axis (MN/m)	3
The stiffness coefficient of the primary suspension along Z-axis (MN/m)	1.04
The stiffness coefficient of the secondary suspension along X-axis (MN/m)	0.24
The stiffness coefficient of the secondary suspension along Y-axis (MN/m)	0.24
The stiffness coefficient of the secondary suspension along Z-axis (MN/m)	0.4
The damping coefficient of the primary suspension along Z-axis (kN·s/m)	30
The damping coefficient of the secondary suspension along Y-axis (kN·s/m)	30
The damping coefficient of the secondary suspension along Z-axis (kN·s/m)	40
The semi-longitudinal distance between bogies (m)	8.6875
The semi-longitudinal distance between wheelsets in a bogie (m)	1.25
The wheel radius (m)	0.46

Table A.2
Parameters of the trailer [40].

Parameters (Unit)	Value
The mass of the car body (kg)	44000
The mass of the bogie (kg)	2400
The mass of the wheelset (kg)	2400
The moment of inertia of the car body about X-axis (kg·m^2)	100000
The moment of inertia of the car body about Y-axis (kg·m^2)	2700000
The moment of inertia of the car body about Z-axis (kg·m^2)	2700000
The moment of inertia of the bogie about X-axis (kg·m^2)	1800
The moment of inertia of the bogie about Y-axis (kg·m^2)	2200
The moment of inertia of the bogie about Z-axis (kg·m^2)	2800
The moment of inertia of the wheelset about X-axis (kg·m^2)	1100
The moment of inertia of the wheelset about Y-axis (kg·m^2)	200
The moment of inertia of the wheelset about Z-axis (kg·m^2)	1100
The stiffness coefficient of the primary suspension along X-axis (MN/m)	9
The stiffness coefficient of the primary suspension along Y-axis (MN/m)	5
The stiffness coefficient of the primary suspension along Z-axis (MN/m)	0.7
The stiffness coefficient of the secondary suspension along X-axis (MN/m)	0.28
The stiffness coefficient of the secondary suspension along Y-axis (MN/m)	0.28
The stiffness coefficient of the secondary suspension along Z-axis (MN/m)	0.3
The damping coefficient of the primary suspension along Z-axis (kN·s/m)	40
The damping coefficient of the secondary suspension along Y-axis (kN·s/m)	25
The damping coefficient of the secondary suspension along Z-axis (kN·s/m)	45
The semi-longitudinal distance between bogies (m)	8.6875
The semi-longitudinal distance between wheelsets in a bogie (m)	1.25
The wheel radius (m)	0.46

Table A.3
Parameters of the ballstless track system (CRTS III) [40].

Parameters (Unit)	Value
Elastic modulus of the rail (N/m^2)	2.059×10^{11}
Torsional inertia of the rail (m^4)	3.741×10^{-5}
Rail second moment of area about the Y-axis (m^4)	3.217×10^{-5}
Rail second moment of area about the Z-axis (m^4)	5.24×10^{-6}

(*continued on next page*)

Table A.3 (*continued*)

Parameters (Unit)	Value
Rail torsional stiffness coefficient (N·m/rad)	1.958×10^5
Rail mass per unit length (kg/m)	60.64
Fastener spacing (m)	0.63
Track slab size (m·m·m)	$5.6 \times 2.5 \times 0.21$
Concrete grade for the track slab	C60
Longitudinal characteristics for the slab	Unit
Filling layer thickness (m)	0.09
Elastic modulus of the filling layer (MPa)	3.25×10^4
Baseplate size (m·m)	3.1×0.3
Concrete grade for the track baseplate	C40

Table A.4
Physical and mechanical parameters of the subgrade in transition zone [12,58].

Parameters (Unit)	Value
Thickness of the surface layer (m)	0.4
Thickness of the bottom layer of subgrade (m)	0∼2.3
Thickness of the subgrade body under subgrade bed (m)	0∼2.7
Thickness of the gravel (m)	0∼5
Width of the surface layer (m)	8.6
Slope of the subgrade ($\tan\theta$)	1/1.5
Elastic modulus of the surface layer (MPa)	180
Elastic modulus of the bottom layer of subgrade (MPa)	110
Elastic modulus of the subgrade body under subgrade bed (MPa)	60
Elastic modulus of the gravel (MPa)	500
Poisson ratio of the surface layer	0.27
Poisson ratio of the bottom layer of subgrade	0.3
Poisson ratio of the subgrade body under subgrade bed	0.35
Poisson ratio of the gravel	0.15
Density of the surface layer (kg/m^3)	2000
Density of the bottom layer of subgrade (kg/m^3)	1800
Density of the subgrade body under subgrade bed (kg/m^3)	1700
Density of gravel (kg/m^3)	1500

Table A.5
Parametric values of prediction model [26,43].

Parameters	The surface layer	The bottom layer of subgrade	The subgrade body under subgrade bed	The gravel layer
a	0.52	0.39	0.85	0.52
b	0.15	0.11	0.14	0.15
m	1.49	1.45	1.16	1.47

References

[1] J.M. de, O. Barbosa, A.B. Fărăgău, K.N. van Dalen, M.J.M.M. Steenbergen, Modelling ballast via a non-linear lattice to assess its compaction behaviour at railway transition zones, J. Sound Vib. 530 (2022) 116942, https://doi.org/10.1016/j.jsv.2022.116942.

[2] C. Charoenwong, D.P. Connolly, P.K. Woodward, P. Galvín, P.Alves Costa, Analytical forecasting of long-term railway track settlement, Comput. Geotech. 143 (2022) 104601, https://doi.org/10.1016/j.compgeo.2021.104601.

[3] B. Indraratna, M. Babar Sajjad, T. Ngo, A. Gomes Correia, R. Kelly, Improved performance of ballasted tracks at transition zones: a review of experimental and modelling approaches, Transp. Geotech. 21 (2019) 100260, https://doi.org/10.1016/j.trgeo.2019.100260.

[4] R. Sañudo, L. dell'Olio, J.A. Casado, I.A. Carrascal, S. Diego, Track transitions in railways: a review, Constr. Build. Mater. 112 (2016) 140–157, https://doi.org/10.1016/j.conbuildmat.2016.02.084.

[5] X. Lei, L. Mao, Dynamic response analyses of vehicle and track coupled system on track transition of conventional high speed railway, J. Sound Vib. 271 (2004) 1133–1146, https://doi.org/10.1016/S0022-460X(03)00570-4.

[6] D. Li, D. Otter, G. Carr, Railway bridge approaches under heavy axle load traffic: problems, causes, and remedies, Proc. Inst. Mech. Eng. Part F J. Rail Rapid Transit. 224 (2010) 383–390, https://doi.org/10.1243/09544097JRRT345.

[7] K.K. Ang, J. Dai, Response analysis of high-speed rail system accounting for abrupt change of foundation stiffness, J. Sound Vib. 332 (2013) 2954–2970, https://doi.org/10.1016/j.jsv.2013.01.005.

[8] A.B. Fărăgău, T. Mazilu, A.V. Metrikine, T. Lu, K.N. van Dalen, Transition radiation in an infinite one-dimensional structure interacting with a moving oscillator—The Green's function method, J. Sound Vib. 492 (2021) 115804, https://doi.org/10.1016/j.jsv.2020.115804.

[9] H. Wang, V. Markine, Dynamic behaviour of the track in transitions zones considering the differential settlement, J. Sound Vib. 459 (2019) 114863, https://doi.org/10.1016/j.jsv.2019.114863.

[10] P. Chumyen, D.P. Connolly, P.K. Woodward, V. Markine, The effect of soil improvement and auxiliary rails at railway track transition zones, Soil Dyn. Earthq. Eng. 155 (2022) 107200, https://doi.org/10.1016/j.soildyn.2022.107200.

[11] A. Jain, A.V. Metrikine, M.J.M.M. Steenbergen, K.N. van Dalen, Railway transition zones: evaluation of existing transition structures and a newly proposed transition structure, Int. J. Rail Transp. 0 (2023) 1–21, https://doi.org/10.1080/23248378.2023.2272668.

[12] Y. Shan, X. Li, S. Zhou, Multi-objective optimisation methodology for stiffness combination design of bridge-embankment transition zones in high-speed railways, Comput. Geotech. 155 (2023) 105242, https://doi.org/10.1016/j.compgeo.2022.105242.

[13] D. Mishra, E. Tutumluer, H. Boler, J.P. Hyslip, T.R. Sussmann, Railroad track transitions with multidepth deflectometers and strain gauges, Transp. Res. Rec. J. Transp. Res. Board 2448 (2014) 105–114, https://doi.org/10.3141/2448-13.
[14] H. Wang, L. Chang, V. Markine, Structural health monitoring of railway transition zones using satellite radar data, Sensors 18 (2018) 413, https://doi.org/10.3390/s18020413.
[15] Y. SATO, Japanese studies on deterioration of ballasted track, Veh. Syst. Dyn. 24 (1995) 197–208, https://doi.org/10.1080/00423119508969625.
[16] Z. Okabe, N. Yasuyama, Laboratory investigation of railroad sub-ballast (second progress report), in: 1961. https://www.semanticscholar.org/paper/Laboratory-Investigation-of-Railroad-Sub-Ballast-(-Okabe-Yasuyama/811ac4fac74807953f678cfb3e958a9be18359a7 (accessed March 27, 2024).
[17] M.J. Shenton, Ballast deformation and track deterioration >, in: TRACK Technol., Thomas Telford Publishing, 1985: pp. 253–265. 10.1680/tt.02289.0026.
[18] C. Monismith, N. Ogawa, C. Freeme, Permanent deformation characteristics of subgrade soils due to repeated loading, Transp. Res. Rec. (1975). https://www.semanticscholar.org/paper/PERMANENT-DEFORMATION-CHARACTERISTICS-OF-SUBGRADE-Monismith-Ogawa/8279210b47859523b6b2920067334f1776d63834. accessed March 27, 2024.
[19] H.E. Stewart, Permanent strains from cyclic variable-amplitude loadings, J. Geotech. Eng. 112 (1986) 646–660, https://doi.org/10.1061/(ASCE)0733-9410(1986)112:6(646).
[20] D. Li, E.T. Selig, Cumulative plastic deformation for fine-grained subgrade soils, J. Geotech. Eng. 122 (1996) 1006–1013, https://doi.org/10.1061/(ASCE)0733-9410(1996)122:12(1006).
[21] X. Bian, H. Jiang, Y. Chen, Accumulative deformation in railway track induced by high-speed traffic loading of the trains, Earthq. Eng. Eng. Vib. 9 (2010) 319–326, https://doi.org/10.1007/s11803-010-0016-2.
[22] J.C.O. Nielsen, X. Li, Railway track geometry degradation due to differential settlement of ballast/subgrade – numerical prediction by an iterative procedure, J. Sound Vib. 412 (2018) 441–456, https://doi.org/10.1016/j.jsv.2017.10.005.
[23] K. Nasrollahi, J.C.O. Nielsen, E. Aggestam, J. Dijkstra, M. Ekh, Prediction of long-term differential track settlement in a transition zone using an iterative approach, Eng. Struct. 283 (2023) 115830, https://doi.org/10.1016/j.engstruct.2023.115830.
[24] I. Grossoni, W. Powrie, A. Zervos, Y. Bezin, L. Le Pen, Modelling railway ballasted track settlement in vehicle-track interaction analysis, Transp. Geotech. 26 (2021) 100433, https://doi.org/10.1016/j.trgeo.2020.100433.
[25] H. Wang, V. Markine, Modelling of the long-term behaviour of transition zones: prediction of track settlement, Eng. Struct. 156 (2018) 294–304, https://doi.org/10.1016/j.engstruct.2017.11.038.
[26] Y. Shan, S. Zhou, H. Zhou, B. Wang, Z. Zhao, Y. Shu, Z. Yu, Iterative method for predicting uneven settlement caused by high-speed train loads in transition-zone subgrade, Transp. Res. Rec. 2607 (2017) 7–14, https://doi.org/10.3141/2607-02.
[27] C. Charoenwong, D.P. Connolly, A. Colaço, P.Alves Costa, P.K. Woodward, A. Romero, P. Galvín, Railway slab vs ballasted track: a comparison of track geometry degradation, Constr. Build. Mater. 378 (2023) 131121, https://doi.org/10.1016/j.conbuildmat.2023.131121.
[28] W. Wang, Z. Li, L. Xu, X. Wei, Modelling and analysis of train-track-subgrade-soil dynamic interaction subjected to the interfacial damage of slab induced by uneven settlement, Appl. Math. Model. 134 (2024) 471–499, https://doi.org/10.1016/j.apm.2024.06.019.
[29] B. Peng, X. He, L. Xu, Z. Li, Y. Guo, Riding safety prediction of a high-speed train running on transition zone under foundation settlement, Adv. Eng. Softw. 197 (2024) 103757, https://doi.org/10.1016/j.advengsoft.2024.103757.
[30] A. Paixão, J.N. Varandas, E. Fortunato, Dynamic behavior in transition zones and long-term railway track performance, Front. Built. Environ. 7 (2021), https://doi.org/10.3389/fbuil.2021.658909.
[31] P. Jiang, L. Ling, Y. Miao, W. Zhai, Experimental and numerical investigation of the track structure elasticity induced by resilient fastener on vehicle-track interaction and train running stability, Eng. Struct. 319 (2024) 118836, https://doi.org/10.1016/j.engstruct.2024.118836.
[32] J. Wang, L. Ling, X. Ding, K. Wang, W. Zhai, The influence of aerodynamic loads on carbody low-frequency hunting of high-speed trains, Int. J. Struct. Stab. Dyn. 22 (2022) 2250145, https://doi.org/10.1142/S0219455422501450.
[33] P.A. Montenegro, H. Carvalho, D. Ribeiro, R. Calçada, M. Tokunaga, M. Tanabe, W.M. Zhai, Assessment of train running safety on bridges: a literature review, Eng. Struct. 241 (2021) 112425, https://doi.org/10.1016/j.engstruct.2021.112425.
[34] Y. Yang, L. Ling, C. Wang, Z. Liu, K. Wang, W. Zhai, Wheel/rail dynamic interaction induced by polygonal wear of locomotive wheels, Veh. Syst. Dyn. 60 (2022) 211–235, https://doi.org/10.1080/00423114.2020.1807572.
[35] J. Zeng, P. Wu, Study on the wheel/rail interaction and derailment safety, Wear 265 (2008) 1452–1459, https://doi.org/10.1016/j.wear.2008.01.031.
[36] P. Wang, J. Wang, X. Ma, D. Ma, J. Xu, Y. Qian, Theoretical 3D model for quasistatic critical derailment coefficient of railway vehicles and a simplified formula, Math. Probl. Eng. (2018) 1–13, https://doi.org/10.1155/2018/7910753, 2018.
[37] Y. Guo, W. Zhai, Y. Sun, A mechanical model of vehicle-slab track coupled system with differential subgrade settlement, Struct. Eng. Mech. 66 (2018) 15–25.
[38] J. Ren, W. Liu, W. Du, J. Zheng, H. Wei, K. Zhang, W. Ye, Identification method for subgrade settlement of ballastless track based on vehicle vibration signals and machine learning, Constr. Build. Mater. 369 (2023) 130573, https://doi.org/10.1016/j.conbuildmat.2023.130573.
[39] M. Chen, S. Zhu, W. Zhai, Y. Sun, Q. Zhang, Inversion and identification of vertical track irregularities considering the differential subgrade settlement based on fully convolutional encoder-decoder network, Constr. Build. Mater. 367 (2023) 130057, https://doi.org/10.1016/j.conbuildmat.2022.130057.
[40] W. Xu, Y. Guo, M. You, Intelligent identification of differential subgrade settlement of ballastless track system based on vehicle dynamic responses and 1D-CNN approach, Transp. Geotech. 48 (2024) 101302, https://doi.org/10.1016/j.trgeo.2024.101302.
[41] L. Xu, W. Zhai, Z. Chen, On use of characteristic wavelengths of track irregularities to predict track portions with deteriorated wheel/rail forces, Mech. Syst. Signal. Process. 104 (2018) 264–278, https://doi.org/10.1016/j.ymssp.2017.10.038.
[42] J.N. Varandas, P. Hölscher, M.A.G. Silva, Settlement of ballasted track under traffic loading: application to transition zones, Proc. Inst. Mech. Eng. F J. Rail Rapid 228 (2014) 242–259, https://doi.org/10.1177/0954409712471610.
[43] Y. Guo, W. Zhai, Long-term prediction of track geometry degradation in high-speed vehicle–ballastless track system due to differential subgrade settlement, Soil Dyn. Earthq. Eng. 113 (2018) 1–11, https://doi.org/10.1016/j.soildyn.2018.05.024.
[44] L. Xu, W. Zhai, Z. Li, A coupled model for train-track-bridge stochastic analysis with consideration of spatial variation and temporal evolution, Appl. Math. Model. 63 (2018) 709–731, https://doi.org/10.1016/j.apm.2018.07.001.
[45] L. Xu, W. Zhai, A three-dimensional dynamic model for train-track interactions, Appl. Math. Model. 76 (2019) 443–465, https://doi.org/10.1016/j.apm.2019.04.037.
[46] W. Zhai, K. Wang, C. Cai, Fundamentals of vehicle–track coupled dynamics, Veh. Syst. Dyn. 47 (2009) 1349–1376, https://doi.org/10.1080/00423110802621561.
[47] Z.C. Zhang, J.H. Lin, Y.H. Zhang, Y. Zhao, W.P. Howson, F.W. Williams, Non-stationary random vibration analysis for train–bridge systems subjected to horizontal earthquakes, Eng. Struct. 32 (2010) 3571–3582, https://doi.org/10.1016/j.engstruct.2010.08.001.
[48] Z. Li, L. Xu, W. Wang, A method for vehicle–track–soil interaction analysis considering soil deformation, Arch. Civ. Mech. Eng. 22 (2022) 210, https://doi.org/10.1007/s43452-022-00518-1.
[49] D.R.M. Milne, L.M. Le Pen, D.J. Thompson, W. Powrie, Properties of train load frequencies and their applications, J. Sound Vib. 397 (2017) 123–140, https://doi.org/10.1016/j.jsv.2017.03.006.
[50] Z. Jin, W. Zhang, Y. Li, X. Geng, Numerical studies of ballastless track-embankment vibrations considering track irregularities, Transp. Geotech. 51 (2025) 101536, https://doi.org/10.1016/j.trgeo.2025.101536.
[51] S. Lei, Y. Ge, Q. Li, Effect and its mechanism of spatial coherence of track irregularity on dynamic responses of railway vehicles, Mech. Syst. Signal. Process. 145 (2020) 106957, https://doi.org/10.1016/j.ymssp.2020.106957.
[52] T. Endo, K. Mitsunaga, K. Takahashi, K. Kobayashi, M. Matsuisht, Damage evaluation of metals for random or varying loading - three aspects of rain flow method, in: Proceedings of the Symposium Mechanical Behavior of Materials, 1974, pp. 371–380.
[53] L. Dong, Research on dynamic characteristics of high-speed railway subgrade and deformation properties under cyclic train load (in Chinese)., (2008).

[54] D. Cojocaru, A. Karlsson, A simple numerical method of cycle jumps for cyclically loaded structures, Int. J. Fatigue 28 (2006) 1677–1689, https://doi.org/10.1016/j.ijfatigue.2006.01.010.
[55] I. Daubechies, Ten lectures on wavelets, society for industrial and applied mathematics, 1992. 10.1137/1.9781611970104.
[56] L. Debnath, F.A. Shah, Wavelet Transforms and Their Applications, Birkhäuser, Boston, MA, 2015. 10.1007/978-0-8176-8418-1.
[57] A. Lasisi, N. Attoh-Okine, Principal components analysis and track quality index: a machine learning approach, Transp. Res. Part C Emerg. Technol. 91 (2018) 230–248, https://doi.org/10.1016/j.trc.2018.04.001.
[58] Z. Li, L. Xu, W. Wang, J. Zhang, J. Wang, B. Peng, Z. Zeng, On use of train-track-subgrade dynamic model for investigating the train-induced cumulative deformation of subgrade and its dynamic effects, Appl. Math. Model. 127 (2024) 71–95, https://doi.org/10.1016/j.apm.2023.11.026.